

LUND UNIVERSITY

MASTER THESIS

**Unbiasing entomological kHz
Scheimpflug LIDAR data**

Author: Alexandra Andersson
Supervisor: Mikkel Brydegaard
Co-supervisor: Samuel Jansson



LUND UNIVERSITY
Faculty of Science

Department of Physics
Division of Combustion Physics
Applied molecular spectroscopy and remote sensing
January 11, 2018

ABSTRACT

Insects can be mapped using a method called Scheimpflug Lidar (Light Detection And Ranging). Sending out light in the near infrared range and detecting the backscattered echo, it is possible to resolve flying organisms in range and time. Insect observations can be distinguished from the background signal through adaptive thresholding.

The detected signal will contain two components; one from light that has scattered on the insect body, and the second due to the wing-beats cycles of the insect. Further, the shape of the wing-beat signal may contain several harmonics due to non harmonic motion and specular reflections.

The wing-beat frequency (WBF) of an insect can be found using a parametrization model where the wing-beat component of signal is projected on a number of harmonic functions. Projections using different possible WBF are done, and the frequency that generates the lowest residual is chosen as the WBF of the signal. Previously, the model has been used in short frequency ranges around a WBF estimated from the signal and the power spectrum of the signal since the model is biased towards minimum possible frequency and Nyquist frequency.

In this thesis, three different compensation methods to overcome the frequency preferences of the model has been investigated with promising results. Further, range biasing and detection limits of the system has been investigated, showing that a longer exposure time makes it possible to detect signals with almost five times as low intensity and reduced the apparent size of the insect. Regarding the range biasing, the system generally detects more observations at short ranges due to higher sensitivity. However, when the range increases a higher amount of observations with long transit time is detected.

ACKNOWLEDGEMENTS

I want to thank

- My supervisor Mikkel Brydegaard for giving me the opportunity to be part of an incredible project
- My co-supervisor Samuel Jansson for all the help he has provided, everything he taught me, for an amazing time in Ivory Coast and for his patience every time I screwed up.
- Elin Malmqvist for everything I learned in Ivory Coast, for all the fun moments during the field campaign and for always having her door open for questions.
- Jérémie Zoueu for the opportunity to be part of the field campaign and taking care of us during the time in Africa.
- All the PhD students in Yamoussoukro who were very warm and welcoming and always helped out.
- International Science Program, Uppsala for sponsoring flight tickets to Ivory Coast.
- Physiographical society, Lund for sponsoring the Lidar system.
- FaunaPhotonics, Danish Innovation Fond and Ifakara Health Insitute for sponsoring Tanzania campaign.
- CAnMove, Lund Laser Centre and LU for general support.
- My boyfriend Anton Linnér for his support and encouragement.
- Jonas Ravelid, Vassily Kornienko and Josefin Kylli for your support and your help with feedback on the report and presentation.
- My colleagues in the Physics and Lazershow - without you I would not have had such a fun time these five years.
- My friends and family for all the support and encouragement.

ABBREVIATIONS

DoF_{reg}	Degrees of freedom in regressor
DoF_{body}	Degrees of freedom in envelope
FoV	Field of view
OCS	Optical cross-section
PoF	Plane of sharp focus
ToF	Time of flight
WBF	Wing beat frequency

SYMBOLS

Symbol	Quantity	Unit
a	Apparent size	[mm]
B_p	Pixel - receiver optics distance	[mm]
C	Linear regression coefficient	[mm ²]
d	Tissue path length	[mm]
D_{rec}	Diameter of receiver telescope	[mm]
D_{trans}	Diameter of transmitting telescope	[mm]
f_{min}	Minimum observable frequency for an observation	[Hz]
f_{max}	Maximum observable frequency for an observation	[Hz]
f_i	Test frequency i	[Hz]
f_N	Nyqvist frequency	[Hz]
f_{sample}	Sample frequency	[Hz]
F_{rec}	Focal length of receiver telescope	[mm]
F_{trans}	Focal length of transmitting telescope	[mm]
g	Anisotropy factor	-
h_{max}	Number of sine/cosine functions in regressor	[#]
H_{pix}	Pixel height	[μ m]
I	Intensity	[uint16]
l	Number of time samples of observation signal	[#]
L	Baseline separation	[mm]
N_{pix}	Number of pixels	[#]
p	Pixel number	-
P_0	Laser power	[W]
r	Distance	[m]
R_{term}	Reflectance of termination target	[%]
Res_i	Sum of squared residual for test frequency f_i	[mm ²]
Res_{body}	Body residual	[mm ²]
$\hat{R}es_{body}$	Analytical body residual	[mm ²]
Res_{regr}	Regressor residual	[mm ²]
$\hat{R}es_{regr}$	Analytical regressor residual	[mm ²]
Res_{tot}	Total residual	[mm ²]
$\hat{R}es_{tot}$	Analytical total residual	[mm ²]
S	Laser spot size	[mm ²]
Δt	Observation transit time	[ms]
τ	Wing-beat period	[ms]
W	Size of sliding minimum	[#]
W_{pix}	Pixel width	[μ m]

δ_{pix}	Pixel coverage	[#]
γ_p	Observed scattering angles	[°]
λ	Central wavelength of laser	[nm]
μ_a	Absorption coefficient	[cm ⁻¹]
μ_e	Extinction coefficient	[cm ⁻¹]
μ_s	Scattering coefficient	[cm ⁻¹]
$\mu_{s'}$	Reduced scattering coefficient	[cm ⁻¹]
σ_{obs}	Optical cross-section for observation	[mm ²]
$\hat{\sigma}$	Least squares fit of observation signal	[mm ²]
ϕ	Swing angle	[°]
$\Phi_{l,1+2h_{max}}$	Regressor of harmonics	-
θ	Tilt angle of sensor	[°]

CONTENTS

1	INTRODUCTION	1
1.1	Medical and ecological background	1
1.2	Entomological Lidar	2
1.3	Modulation spectroscopy	3
1.4	Aim	4
2	LIGHT-TISSUE INTERACTION	5
2.1	Single scattering events	5
2.2	Multiple scattering in tissue	5
2.3	Light-insect interaction	6
3	INSTRUMENTATION	9
3.1	Scheimpflug lidar	9
3.2	Experimental setup	10
3.3	Range calibration	11
4	DATA ANALYSIS	13
4.1	Raw data processing	13
4.1.1	Insect thresholding and extraction	13
4.1.2	OCS and apparent size calibration	15
4.2	Finding the fundamental wing beat frequency	16
4.2.1	Parameterization model	16
4.2.2	Frequency preference of the model	19
4.2.3	Fine tuning	22
5	FIELD CAMPAIGNS	25
5.1	Ivory Coast field campaign	25
5.2	Tanzania field campaign	27
6	RESULTS	29
6.1	Detection limit	29
6.2	Range biasing	30
6.3	Frequency preference compensation	33
7	DISCUSSION	37
7.1	Detection limit	37

7.2	Range biasing	37
7.3	Frequency preference compensation	38
8	CONCLUSIONS AND OUTLOOK	41

Chapter 1

INTRODUCTION

1.1 Medical and ecological background

Malaria is one of the diseases that kill most people over the world today. In 2015 almost 450 000 people died [1] which makes the malaria mosquito the deadliest animal in the world.

Mosquitoes normally feed on nectar, but in several mosquito species the females need human blood to produce eggs. After mating the females seek a human host for blood by following the body odor (CO_2 , ocentanol). After feeding on blood, the females rest for a couple of days while digesting the bloodmeal and develop eggs. When the females have laid their eggs, in or close to water, the reproduction cycle repeats until the female dies [2].

A mosquito can only be infected by malaria by feeding on a human host who bears the malaria parasite. The parasite does not transmit to the eggs, so a human is only infected if they are bit by a mosquito that has fed on a malaria infected host in a previous instance [3]. A mosquito lives roughly 2 weeks in nature, meaning that the females only mate once, maybe twice, in their lifetime. The probability that the mosquito both has been infected and has mated twice is small, but due to the large number of mosquitoes, there are over 200 million malaria cases every year [1].

Unfortunately, there is no fully protecting vaccine or medicine for malaria today. The main product is malaria prophylaxes which serves both as vaccine and medicine. However, some parasites have become resistant to some prophylaxes and therefore it is important to do preventative work to avoid malaria. Today the preventative work mainly consists of mosquito spray and bed-net campaigns. Unfortunately, neither the sprays or the nets give full protection; in Tanzania for example, a prevention program [4–6] resulted in the mosquitoes changing their activity pattern during the day.

To be able to do more preventive work like draining of wet areas and urban planning, it is of importance to be able to monitor mosquitoes and their habits, especially since there are several mosquito species that are active in different

areas, at different times of the year, that are infectious to different degree and have different behavior. Further, it is necessary to be able to distinguish the females from the males to get a more more detailed understanding of the ecology of either gender.

The easiest and most common way to monitor mosquitoes is using mosquito traps. Traps can attract mosquitoes in several ways, for example by CO_2 , light traps or human bait. Trapping mosquitoes, it is easy to study how many mosquitoes from different species that are captured in different areas, at different times of the year. The drawbacks with traps are that they might be biased towards some species, it is hard to cover large areas, and they have low time resolution.

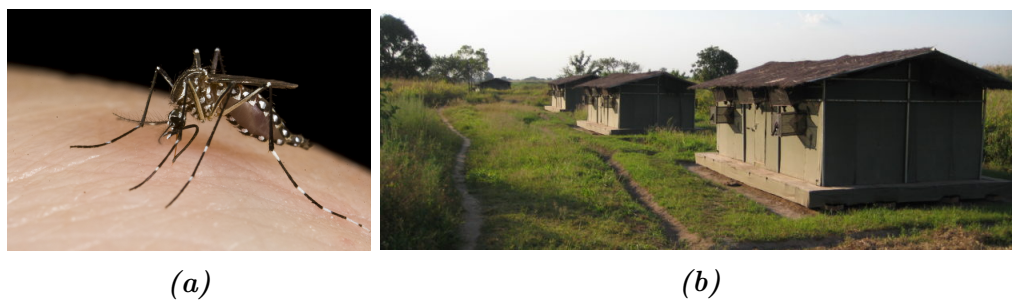


Figure 1.1: **a)** Image of a female *aedes aegypti*. **b)** Image of mosquito traps in Tanzania, [5].

1.2 Entomological Lidar

An alternative to conventional traps is to detect insects using entomological Lidar [7–9], (laser radar), which can be used to detect and map aerosols and particles in the atmosphere by detecting the backscattered echo of a laser [10–13]. For example, entomological Lidar has earlier been used to map insect density and speed [14], and to monitor insect pests in crops [15, 16].

A Lidar setup usually consist of a laser connected to an expanding telescope, and a receiving telescope that focuses the backscattered light onto a detector. Using a pulsed laser, the echoes can be range resolved using time of flight (ToF) [17–21] as illustrated in Figure 1.2.

Apart from the pulsed laser technique, another method for range resolved Lidar using a continuous laser can be used [2, 22]. However, this was previously pursued using a telescope baseline separation between the telescopes in the order of hundreds of meters and hence a wide angle objective is required. Unfortunately, the aperture size is compromised when the acceptance angle is high which means a lower light collection efficiency. To be able to detect insect echoes from the full range of the laser beam with a compact setup, at a low cost and with high efficiency, a method called Scheimpflug Lidar, that uses the Scheimpflug principle [23, 24] has been used [25].

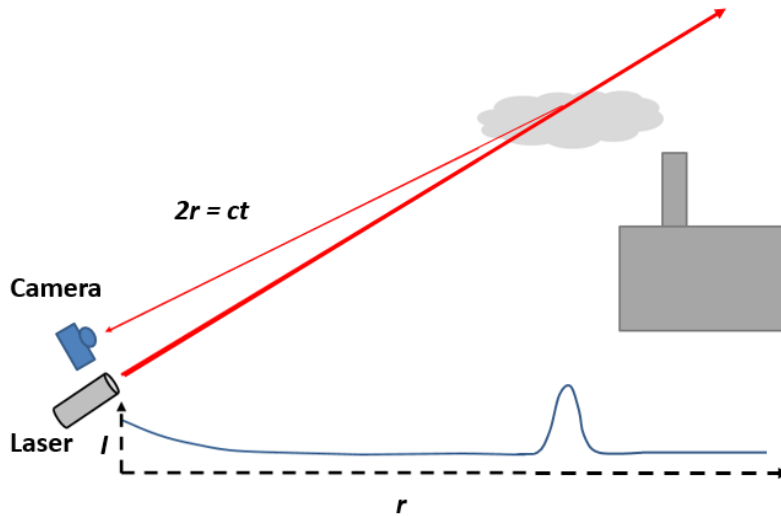


Figure 1.2: Image of the concept of atmospheric Lidar.

1.3 Modulation spectroscopy

The detected insect signal will contain a component due to the light scattered on the body of the insect, as well as a component due to light scattered on the beating wings [26–30]. The fundamental wing-beat frequency, (WBF), which can vary in a range between 10-1000 kHz depending on insect species [31] depend on the flight speed, acceleration and ambient temperature [32–35].

The wing-beat signal may contain several harmonics due to harmonic motion and specular reflections [36]. The full modulation spectra of insects has been studied using an electro-optical tool [37–39] and can be used for insect classification [37] since species with similar fundamental WBF can vary in harmonic content, as can be seen in Figure 1.3.

Comparing mosquitoes to other insects, mosquitoes have a higher WBF than several other species. Female mosquitoes typically have a WBF around 400-600 Hz and males around 600-800 Hz [40, 41].

The fundamental WBF of the signal can be found using a model trying to fit a number of harmonics containing the WBF to the signal. Since the WBF is unknown, a vector with test frequencies is defined. For each test frequency the body signal is obtained with a sliding minimum filter given by the test frequency. A regressor consisting of a number of harmonics containing the current test frequency and overtones of it is fit to the signal. When all frequencies in the test vector has been tested, the frequency that results in the fit with the lowest residual is chosen as WBF.

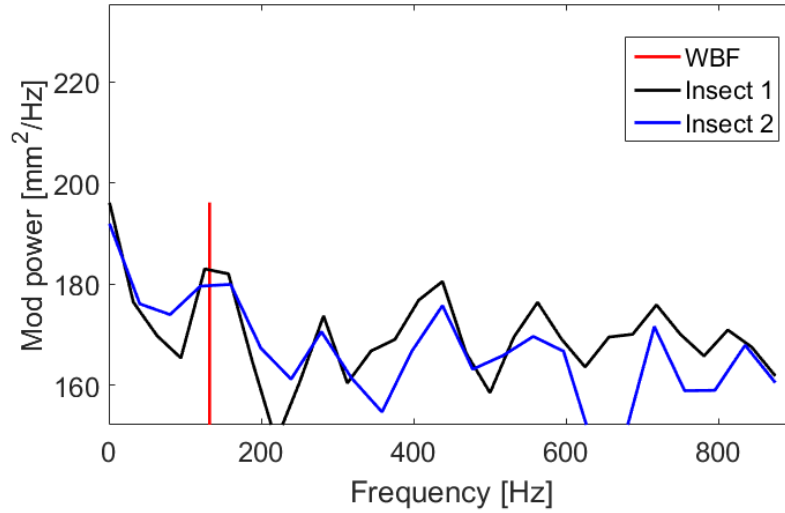


Figure 1.3: Modulation power as a function of frequency for two different insect observations. The two observations have the same WBF but the strength of the overtones differ.

1.4 Aim

The drawback with the described frequency selection method is that the model favors high and low frequencies, which means that it has not been possible to test frequencies in the full range from 1 to the Nyquist frequency with reliable results. Instead, the range of the test frequencies has earlier been limited to a small span around a preliminary WBF obtained from the time series of the insect [42]. The aim of this thesis is to investigate the frequency preference of the model and find a way to compensate for the methodological biasing in the frequency and range domains.

Chapter 2

LIGHT-TISSUE INTERACTION

2.1 Single scattering events

Single scattering of light on particles depends on the particle size. Assuming only elastic scattering, Rayleigh scattering is applicable when considering small particles with a particle diameter much smaller than the wavelength of the light. If the particle diameter is in the same magnitude as the wavelength, or larger, Mie scattering can be used.

The scattering cross-section for Rayleigh scattering is dependent on the wavelength to a factor $\mu_{s,R} \propto 1/\lambda^4$, whereas Mie scattering has a scattering coefficient dependent of the wavelength to a factor $\mu_{s,M} \propto 1/\lambda^2$ [43]. Except for the lower dependence on the wavelength, Mie scattering is highly dependent on the particle size [44], and has a lower fraction of backscattering.

2.2 Multiple scattering in tissue

When illuminating tissue with light, the photons can be transmitted to the tissue where they can undergo multiple scattering and absorption. If the optical properties are known, the propagation of light in tissue can be modeled by the Radiative Transfer Equation, (RTE). The RTE can be solved using the diffusion equation [45] if the sample size is small than the mean free path. In case of larger tissue chromophores, the photomigration in tissue can instead be described by a random walk model [46]. In the model, the probability distributions of the step size and the deflection angle is used to predict the next scattering event.

The distribution of Mie scatterers can be approximated by the Henyey-Greenstein scattering phase function [47].

From the Henyey-Greenstein function, the scattering coefficient, μ_s , that gives the probability of scattering per unit path length, can be obtained. To compensate for the anisotropy, g , the scattering coefficient is most often expressed

as the reduced scattering coefficient

$$\mu'_s = \mu_s(1 - g). \quad (2.1)$$

Absorption can be applied according to Beer Lambert's law,

$$I = I_0 e^{-\mu_a c d}, \quad (2.2)$$

where c is the concentration, d is the path length before absorption, and μ_a is the absorption coefficient giving the probability of absorption per unit path length. The total attenuation in the tissue can be described by the extinction coefficient,

$$\mu_e = \mu'_s + \mu_a. \quad (2.3)$$

2.3 Light-insect interaction

The wings of an insect are thin, (about 400 nm), and dry, and can be described as a multilayer thin film [48] consisting of chitin and melanin. When illuminated, the backscattered light is either a specular reflection from the utmost layer, or a diffuse reflection from the underlying layers. Considering the insect body, the light can be either scattered on the surface, or entering the tissue where the photons undergo multiple scattering and absorption. Since only a fraction of the diffuse light will be scattered 180° , there are losses due to absorption and omni-directionally scattered light.



Figure 2.1: Illustration of losses in intensity due to omni-directional scattering.

The wings beat and will therefore give rise to a strong specular backscattered signal when the wing surface coincide with the optical axis, and a weak signal when coinciding with the laser beam. This results in a signal that consist of a broad constant contribution from the body with high intensity wing-beats on top, as can be seen in Figure 2.2.

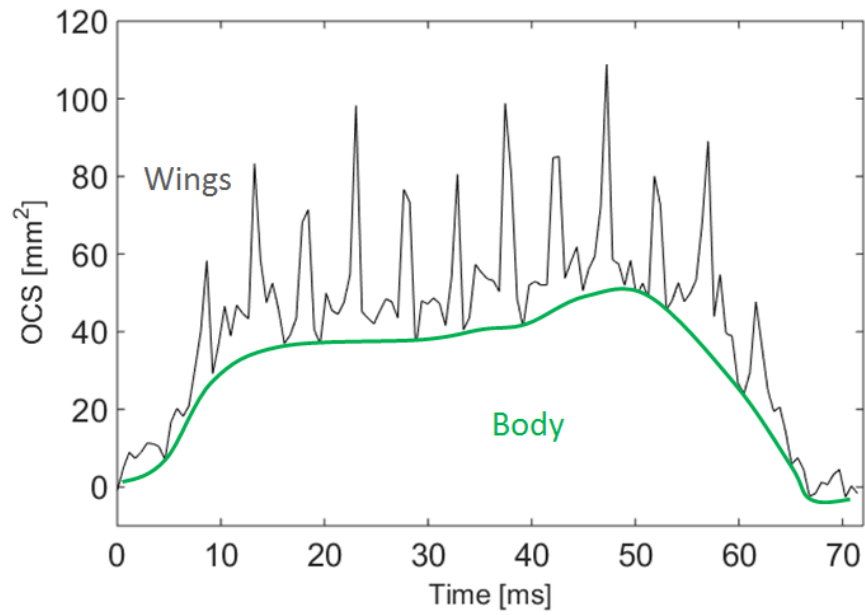


Figure 2.2: Time series of an observation. The signal consists of a signal from the body and the signal from the wings.

Chapter 3

INSTRUMENTATION

3.1 Scheimpflug lidar

Backscattered echoes from different ranges, r , will be projected with sharp focus at different distances, B_p , from the lens plane of the receiving telescope. Echoes from infinite depth are projected on a distance corresponding to the focal length of the receiving telescope, $B_p = F_{rec}$, and as the range decreases, B_p will increase. In order to obtain sharp focus over a long range the Scheimpflug principle [23,24] is implemented in the setup. That is done by placing the first pixel, p_1 , of the line array sensor in the focus of the receiving telescope and then tilt the line array sensor with an angle θ , as can be seen in Figure 3.1. By increasing the length of the sensor, or increasing the tilt angle, θ , to maximum, echoes from shorter ranges can be projected.

The plane of sharp focus, (PoF), is given by the Scheimpflug and Hinge intersects, i.e. a plane where the lens plane and the image plane intersect, as well as two planes parallel to those. The intersects and the geometry of the setup are drawn in Figure 3.1. In case of a Lidar system, the setup has to be arranged so that the PoF coincides with the laser beam [25].

Due to the triangular geometry of the setup, the range resolution of a Scheimpflug Lidar system is tangential. The resolution is limited by the camera pixel size, the telescope baseline separation distance, L , and the field of view, (FoV) of the camera (that increases with range). In comparison to a ToF Lidar system [17–21] where the range resolution is limited by the pulse width, a Scheimpflug system has a higher resolution at short distances. The temporal resolution of the Scheimpflug Lidar system is limited by the read-out-speed of the camera.

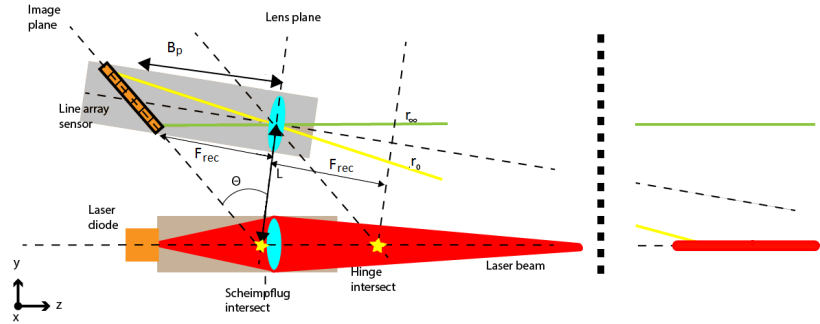


Figure 3.1: Drawing of the setup. Echoes from different ranges, r , are projected with sharp focus at different distances, B_p , from the receiving lens. Hence the image plane, (line array sensor), is tilted by an angle θ , in relation to the laser beam and lens plane of the receiving telescope. The result is that signals from an infinite depth are projected on the first pixel placed in the focal point of the receiving lens, ($B_p = F_{rec}$), and signals from shorter ranges are projected at pixels with a longer B_p . The plane in which sharp focus is obtained, (which should coincide with the laser beam) is given by the Scheimpflug and Hinge intersects, i.e. a plane where the lens plane and the image plane intersect, as well as two planes parallel to those.

3.2 Experimental setup

The setup includes a 808 nm 3.2 W diode laser, transmitting through an expanding refractor telescope (diameter 102 mm and focal length 500 mm). Backscattered light is collected with a Newtonian telescope (diameter 205 mm and focal length 800 mm) and focused onto a line array sensor which is tilted 45 degrees in relation to the optical axis of the receiving telescope. The telescopes are mounted on a telescope mount with a baseline separation distance $L = 814$ mm. To facilitate alignment and focusing, a monitoring camera is mounted between the the telescopes.

The laser, which is aligned horizontally and terminated on a neoprene target with a reflectance of approximately 4%, is connected to a multiplexing driver triggered by the camera strobe. The triggering enables modulated measurements where the laser is intermittently switched on and off between exposures, meaning that every second recorded line will include the backscattered echo from the laser, (on slot), and every second recorded line will be a a recording of the optical background signal, (off slot). The optical background signal is later used to subtract the background from the on slot.

An image of the setup can be seen in Figure 3.2 and the system parameters can be seen in Table 3.1.

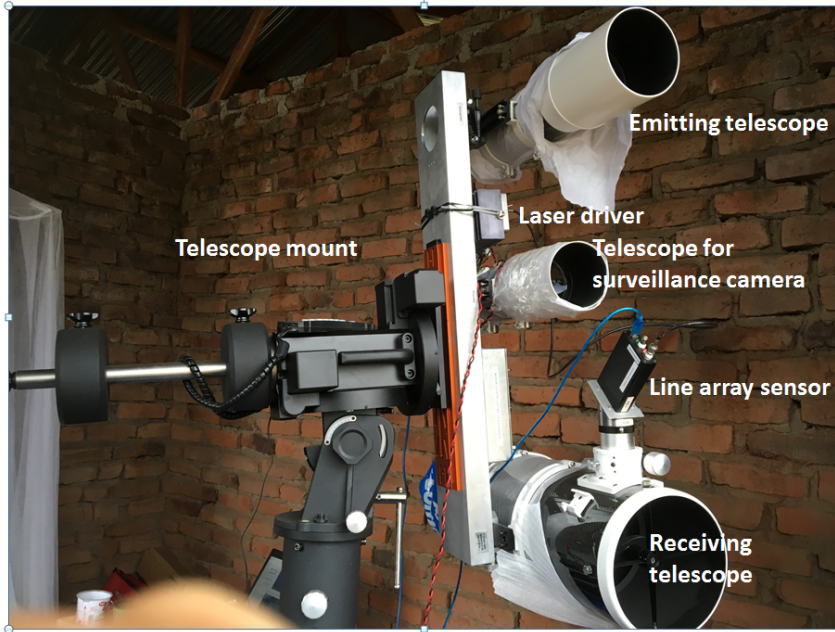


Figure 3.2: Image of the setup when used in the field.

Table 3.1: Table of the system parameters.

Parameter	Symbol	Value [unit]
Receiver telescope focal length	F_{rec}	800 [mm]
Transmitting telescope focal length	F_{trans}	500 [mm]
Receiver telescope diameter	D_{rec}	205 [mm]
Transmitter telescope diameter	D_{trans}	102 [mm]
Baseline separation distance	L	814 [mm]
Laser wavelength	λ	808 [nm]
Laser power	P_0	3.2 [W]
Number of pixels	N_{pix}	2048 [#]
Pixel width	W_{pix}	14 [μm]
Pixel height	H_{pix}	200 [μm]
Reflectance termination plate	R_{term}	4 [%]
Laser spot size	S	233×25 [mm^2]

3.3 Range calibration

The observed scattering angles between the laser beam and a pixel p , is given by

$$\gamma_p = \tan^{-1}(L/r). \quad (3.1)$$

The relation between the distance, r , an echo originates from, and which pixel, p , the echo is projected on is given by

$$r = \frac{L[pW_{pix}(\sin(\theta) - \cos(\theta)\tan(\phi)) + B_p]}{pW_{pix}(\cos(\theta) + \sin(\theta)\tan(\phi)) + B_p\tan(\phi)}. \quad (3.2)$$

where B_p for a pixel p is given by

$$B_p = \frac{r_{term}F_{rec}}{r_{term} - F_{rec}} - pW_{pix}\sin(\theta), \quad (3.3)$$

The swing angle ϕ , i.e. the angle between the laser beam and the receiver axis, is given by

$$\phi = \tan^{-1}(L/r_{term}) - \tan^{-1}\left(\frac{p_{term}W_{pix}\cos(\theta)(r_{term} - F_{rec})}{r_{term}F_{rec}}\right). \quad (3.4)$$

where p_{term} is the pixel on which the echo from the termination plate at distance r_{term} is positioned.

Chapter 4

DATA ANALYSIS

4.1 Raw data processing

The raw data, in 16 bit unsigned integer format, is read into matrices in Matlab, one file containing 10 seconds of collected data at all ranges at a time. The background (off slot) is subtracted from the data (on slot) by subtracting a mean of the two neighboring off slots from every on slot. An image of a typical file during dusk can be seen in Figure 4.1. The insects can be seen as the small yellow dots (high intensities) and the the small regions of higher intensity with a periodic structure arising from the wing beats.

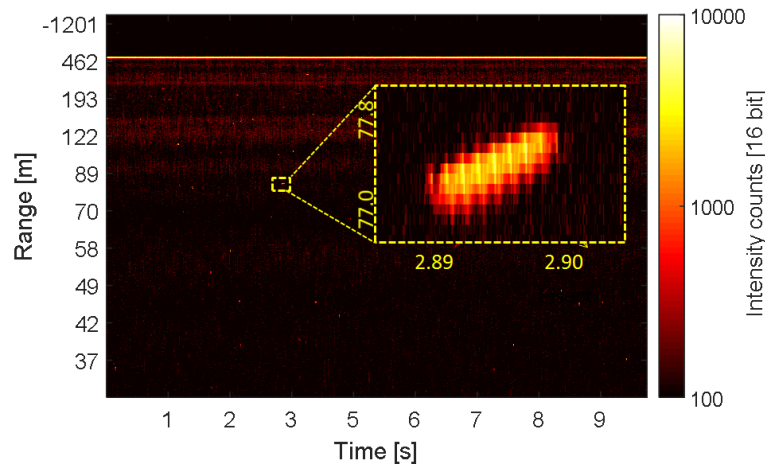


Figure 4.1: From the original time-range map, the insect signals can be seen as small areas with a periodic structure arising from the wing beats.

4.1.1 Insect thresholding and extraction

From the file, the minimum, median and maximum intensities are obtained, as can be seen in Figure 4.2. The threshold for what is considered to be an insect,

corresponding to a signal-to-noise ratio, $SNR = 2$, is set to

$$I_{thresh} = I_{med} + 5 * I_{iqr}, \quad (4.1)$$

where I_{med} is the median and I_{iqr} is the interquartile range intensity of every time sample. A plot of maximum, median and minimum intensities for the same file as in Figure 4.1 can be seen in Figure 4.2.

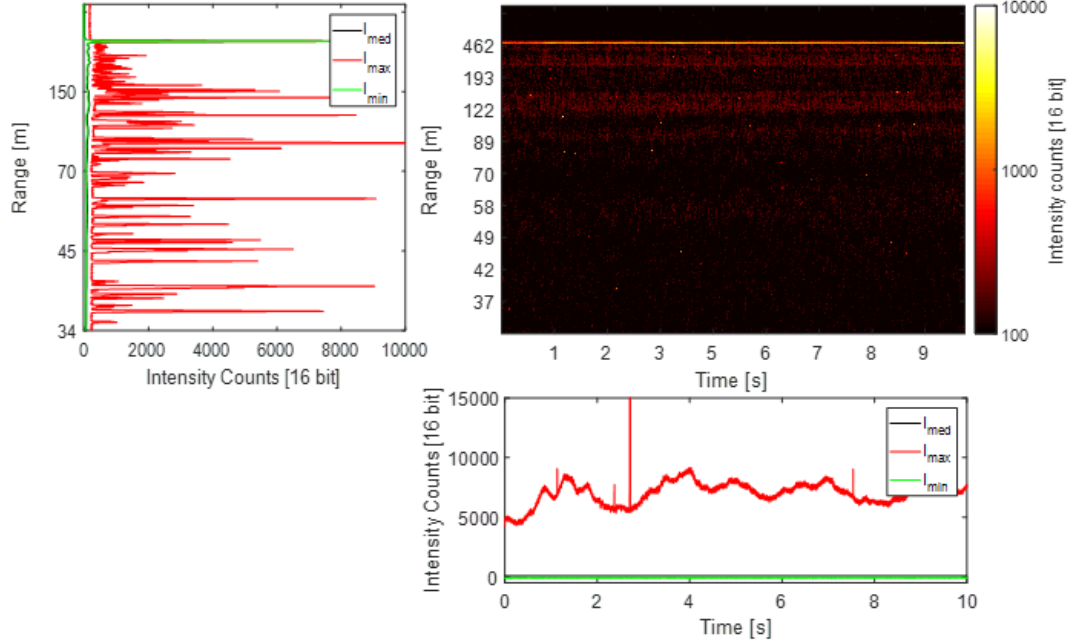


Figure 4.2: The maximum, median and minimum intensities for each time and range can be extracted from the file. This is used to set a threshold for an insect observation intensity.

Identification of positions corresponding to insects in the time-range file are done using a binary mask. The mask maps the positions that have an OCS exceeding the threshold intensity. The edges of the insect area is eroded with a $1 \text{ pixel} \times 3 \text{ time samples}$ window to omit observations that are too short to be analyzed. Further, it is dilated with a $5 \text{ pixel} \times 30 \text{ time samples}$ window to include flanks of observations which are not above threshold and make sure no observations are analyzed twice. The resulting binary mask is used to determine which positions in the original time-range map that are extracted and saved as an insect observation in time and range.

All range pixels associated with one time sample for a specific observation are then summed into a time series. The time series, range-time map and other relevant observation and file parameters are saved into a .mat-file that is used for the frequency analysis. A schematic flowchart of the raw data processing can be seen in Figure 4.3.

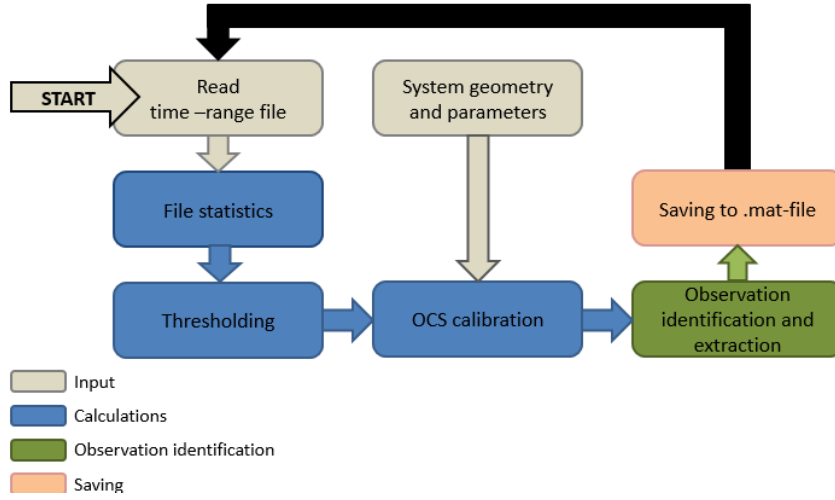


Figure 4.3: The process during the raw data processing starts with reading the files and obtaining the median, minimum and maximum intensities for every time sample in the file. The intensities are converted to OCS, and the insect observations can be identified in OCS using set thresholding and extraction parameters.

4.1.2 OCS and apparent size calibration

The intensity of the time series is calibrated from counts in uint16 to optical cross-section (OCS), σ_{obs} , in units of mm^2 as done by Brydegaard [26, 49–51],

$$\sigma_{obs} = \frac{\sigma_{term} * r_{obs}^2 (I_{obs(r)} - I_{med(r)})}{(I_{med(r)} * r_{term}^2)}. \quad (4.2)$$

where the optical cross-section at the termination can be calculated as

$$\sigma_{term} = S * R_{term}, \quad (4.3)$$

where R is the reflectance of the termination plate and S is the illuminated area on the termination, which can be seen in Figure 4.4.

Further, the size of a detected insect is calibrated in terms of apparent size,

$$a = \frac{r * \cos(\theta) \delta_{pix} W_{pix}}{F_{rec}}, \quad (4.4)$$

where δ_{pix} is the maximum number of range pixels associated with one separate time sample.

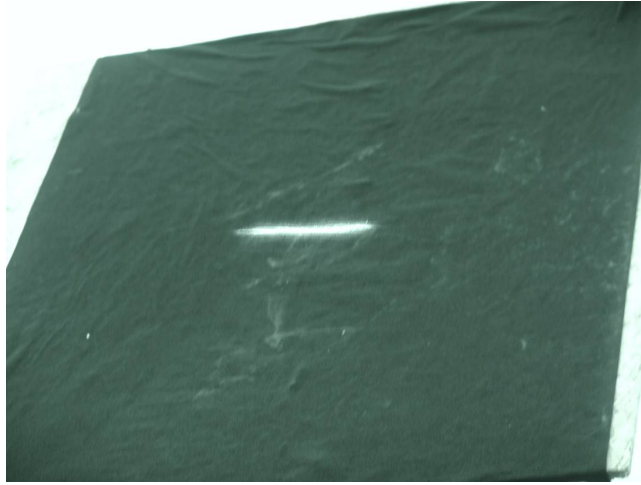


Figure 4.4: Image of the laser spot on the termination plate.

4.2 Finding the fundamental wing beat frequency

The time series will consist of the reflection from the body of the insect and the reflections from the wing beats. There are several ways to find the WBF from a detected time series. The WBF can be estimated by $WBF = \frac{1}{\tau}$ where τ is an estimation of the time between the wing beats [42]. Other methods include using Cepstrum analysis [52], finding the WBF by Hilbert-Huang transform [53], or Fourier transform [42]. In Figure 4.5 a time series and a Fourier transformed time series can be seen, showing the WBF, the transit time, δt , and the wing beat period, τ , [42].

The problem with these methods is that the wing beats in the time series are often irregular, and the power spectra are often noisy and may contain side lobes, which results in a lower frequency than the actual WBF is considered to be the WBF.

4.2.1 Paramerization model

Another way of finding the WBF, developed by Brydegaard [36], is to fit a number of harmonics containing the WBF and overtones to the time series. Since the WBF is unknown, harmonics containing all possible WBF for the observation are fit to the signal, one frequency at a time.

The lowest possible WBF is given by the transit time of the observation. A criterion of three wing-beats within the time series is defined, resulting in a minimum possible WBF, $f_{min} = \frac{3}{\Delta t}$. The maximum possible WBF is the Nyquist frequency $f_N = \frac{f_{sample}}{2}$. When all possible frequencies has been tested, the frequency that yields the fit with the lowest residual is chosen to be the WBF.

For every frequency f_i that is tested, the body contribution, b , of the signal

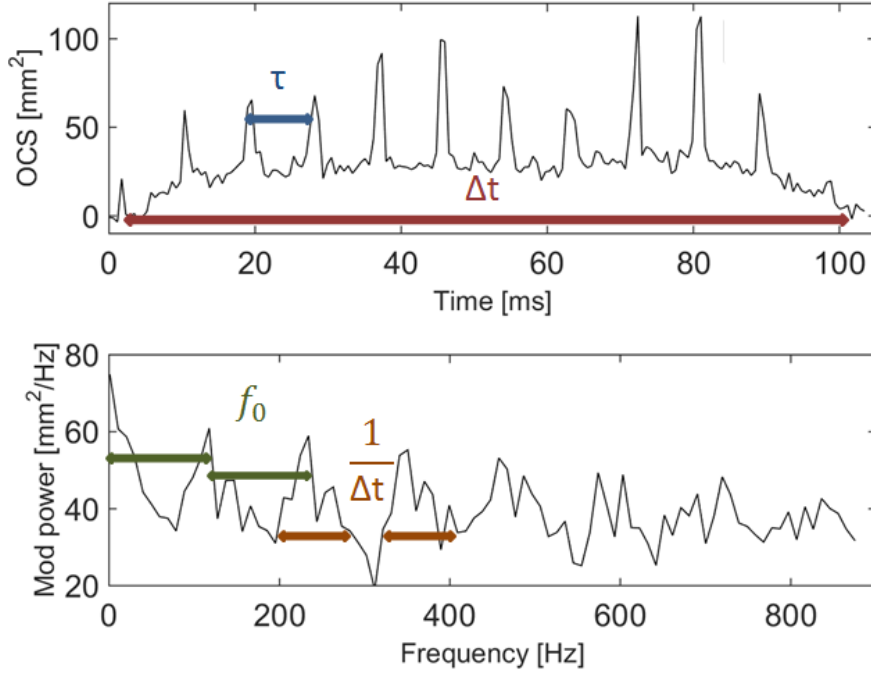


Figure 4.5: The WBF can be obtained using the median peak distance in the power spectrum or by using the time difference between the peaks in the time series.

is obtained using a sliding window that slides through the signal and chooses the lowest value of OCS within the window to represent the body contribution. The window size depends on the current test frequency as $W = \frac{2 * f_N}{f_i}$, rounded to closest integer. The size of the window, W , is related to the degrees of freedom, (DOF's) as

$$DoF_{body} = \frac{l}{W},$$

rounded to closest integer, where l is the number of time samples in the time series. Further, the time series corresponding to the body contribution is smoothed with a Gaussian filter with full width half maximum $FWHM = \frac{W}{2}$, and the noise level of the corresponding time samples are added.

The signal arising from wing beats is the difference between the original time series and the body time series. The wing signal is reconstructed by projecting the time series on a regressor, Φ , consisting of a number of harmonic functions with the current test frequency and overtones of it.

$$\Phi_{l,1+2h_{max}} =$$

$$\begin{bmatrix} b_1 & b_1 \sin(2\pi h_1 f_i t_1) & b_1 \cos(2\pi h_1 f_i t_1) & b_1 \sin(2\pi h_2 f_i t_1) & \dots & b_1 \cos(2\pi h_{max} f_i t_1) \\ b_2 & b_2 \sin(2\pi h_1 f_i t_2) & b_2 \cos(2\pi h_1 f_i t_2) & b_2 \sin(2\pi h_2 f_i t_2) & \dots & b_2 \cos(2\pi h_{max} f_i t_2) \\ \vdots & \vdots & \vdots & \vdots & \ddots & \vdots \\ b_l & b_l \sin(2\pi h_1 f_i t_l) & b_l \cos(2\pi h_1 f_i t_l) & b_l \sin(2\pi h_2 f_i t_l) & \dots & b_l \cos(2\pi h_{max} f_i t_l) \end{bmatrix}$$

The variable

$$h_k = 1, 2, \dots, h_{max} = 1, 2, \dots, \lfloor \frac{f_N}{f_i} \rfloor$$

is a counter, giving the number of sine and cosine functions respectively. By multiplying the current test frequency with h_k , the first sine and cosine functions in the regressor will contain the current frequency being tested as WBF, the second sine and cosine functions contain the first overtone, etc. This means that the number of columns in the regressor, i.e. the degrees of freedom in the regressor, is given by

$$DoF_{regr} = 1 + 2h_{max},$$

corresponding to one unknown constant, h_{max} sine functions and h_{max} cosine functions. Multiplying with $b_{1,2..l}$ corresponds to weighing the regressor with the the OCS contribution from the body. The weighing is done since there would be no signal from the wing beats unless the body of the insect is in the laser beam. An illustration of the weighing of the regressor can be seen in Figure 4.6.

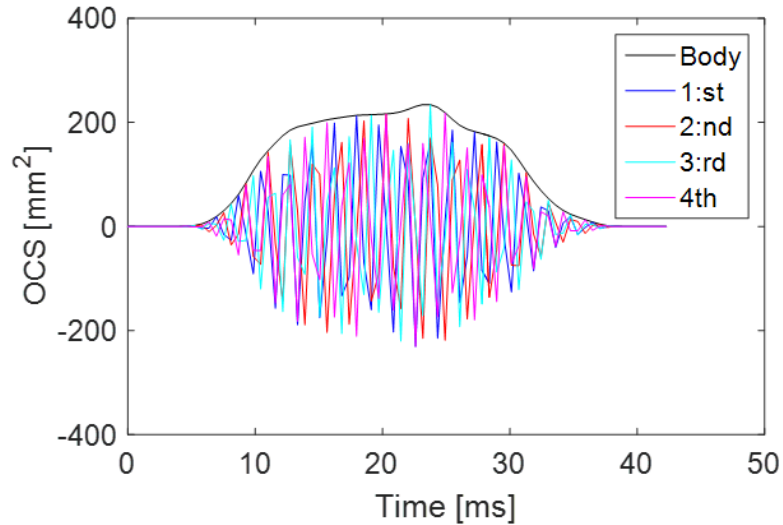


Figure 4.6: Illustration of the weighing effect of the harmonic functions.

Using linear regression, (least squares method),

$$C = (\Phi^T \Phi)^{-1} \Phi \sigma_{obs} \quad (4.5)$$

$$\hat{\sigma} = \Phi \cdot C, \quad (4.6)$$

a fit of the time series is obtained and the sum of squares residual,

$$res_i = \sum_{j=1}^l (\sigma_{obs,j} - \hat{\sigma}_j)^2, \quad (4.7)$$

between the fit and the time series for the current test frequency is saved.

This results in a frequency dependent residual vector, Res_{tot} , with a residual value res_i for every tested frequency, f_i , and the frequency that yield the lowest residual is chosen as WBF.

4.2.2 Frequency preference of the model

If a signal that does not contain any frequency would be seeded into the model, the residual curve should be flat. If a signal containing a frequency is seeded into the model, the expected residual curve should be flat, except for dips corresponding to the frequency of the signal and the overtones of this frequency. Unfortunately the model is biased toward the extremes, it either chooses a high frequency, which is referred to as the right ditch, or a low frequency, referred to as the left ditch, as can be seen in Figure 4.7.

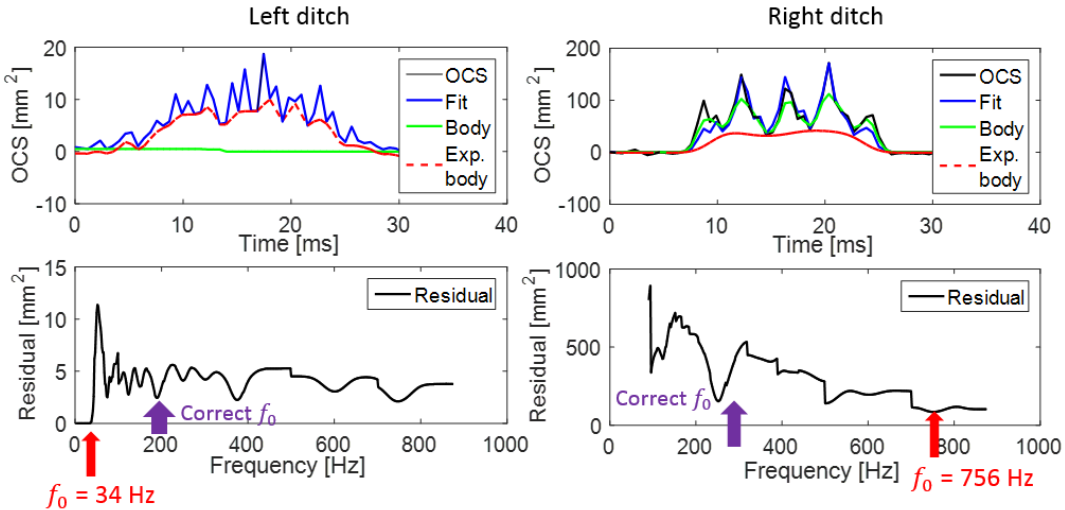


Figure 4.7: Illustration of the two ditches. If the model chooses a low frequency DoF_{reg} is larger than the number of sample points in the time series and a transform is obtained. If the model chooses a high frequency, the window size is small and follows the time series up in the wings.

The frequency preferences of the model is investigated by seeding the parametrization model with 1000 empty observations, (data that does not contain any insect observation and hence no frequency), of different transit times, which can be seen in Figure 4.8.

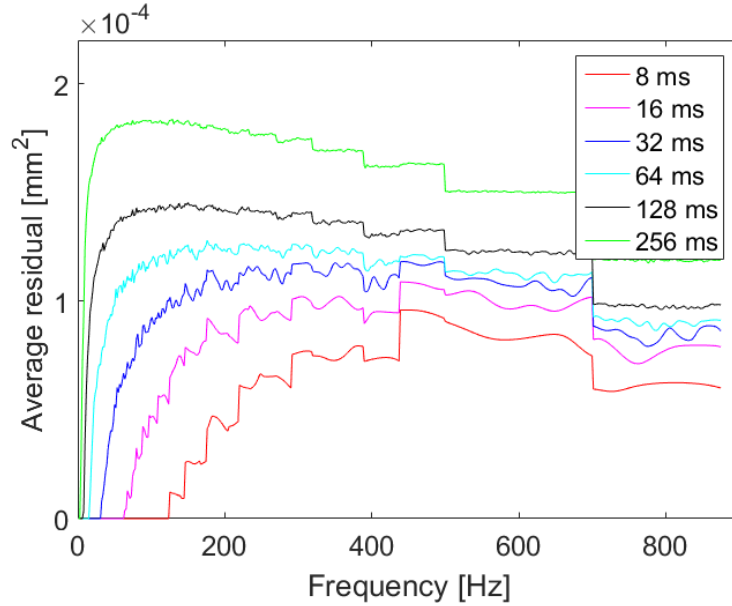


Figure 4.8: Residual vector when seeding data that does not contain any observation into the parametrization model.

The residual curve, Res_{tot} , in Figure 4.8 can be split into two pieces, $Res_{tot} = Res_{body} \cdot Res_{regr}$. Res_{body} arises from the sliding window, i.e. the residual if the body is fit to the signal, and Res_{regr} arises due to the harmonics, i.e. the residual if the regressor would not be weighed with the body. This can be seen in Figure 4.9.

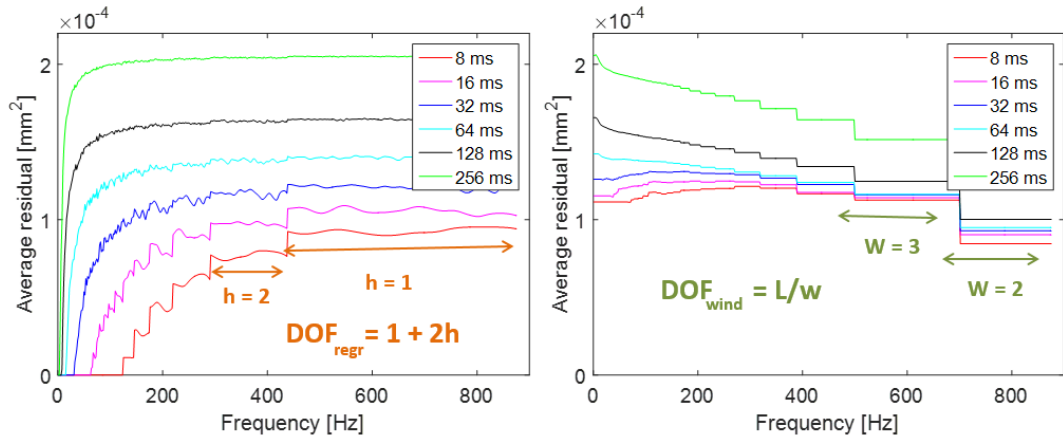


Figure 4.9: **a)** Residual vector from the regressor as a function of frequency. When DoF_{regr} increases for lower frequencies, the residual decreases. **b)** Residual vector from the sliding as a function of frequency. When DoF_{body} increases for higher frequencies, the residual decreases.

As it can be seen from Figure 4.9, the sliding window gives rise to a step

behavior favoring high frequencies. That is a result of the size of the sliding window. The window size can at minimum be 2 time samples, resulting in the lowest value of every second sample point in the time series describing the body. In that case the body time series itself almost describes the original time series. Passing these specific frequencies where the window size changes, for example around 700 Hz where it changes from $W = 2$ to $W = 3$ and the body contribution suddenly is described by every third value in the time series, results in a sudden decrease in DoF_{body} and hence a sharp increase in the residual.

Considering Res_{regr} there is a similar step behavior. The steps are decreasing towards lower frequencies as a result of an increasing DoF_{regr} . For frequencies up to $f_i = \frac{1}{\tau}$, DoF_{regr} is larger than the number of sample points in the time series. Hence there will be one or more harmonics to describe every point in the time series, and the fit is a transform yielding zero residual. The shorter transit the time of the observation, the higher the lowest observable frequency that yields a transform becomes.

In order to properly determine the wing-beat frequency in an insect signal, the frequency preferences of the model have to be evaluated and accounted for. Three main alternatives to compensate for frequency preferences have been investigated in this thesis; using an general analytic function, observation specific function, and lifting up the residual curve at every DoF_{regr} change or change in window size.

Compensation method - Analytic function

The first alternative is to use an analytic expression to reconstruct the step behavior of the residual curve,

$$\hat{Res}_{tot} = \hat{Res}_{regr} \cdot \hat{Res}_{body} = \left(1 - \frac{DoF_{regr}}{l}\right) \cdot \left(1 - \frac{DoF_{body}}{l}\right). \quad (4.8)$$

The resulting analytical function for an observation with $l = 100$ can be seen in Figure 4.10.

The original residual curve is then divided by the analytical function in order to compensate for the preferences towards low and high frequencies.

Compensation method - Analytical function using Res_{body}

The second alternative is to compensate for the preferences towards high frequencies by division between the original residual curve and the body residual Res_{body} . The preference towards lower frequencies cannot be compensated for in the same manner by division with Res_{regr} , since that would erase the dips for matching WBF as well. Instead, the step shape of Res_{regr} is found by fitting Res_{regr} to the analytical function describing the regressor residual in the previous method, multiplied with an extra factor in order to better match the observation specific shape. The final expression is described as

$$\hat{Res}_{tot,i} = \left(1 - \frac{DoF_{regr,i}}{l}\right) \cdot l^c \cdot Res_{body}, \quad (4.9)$$

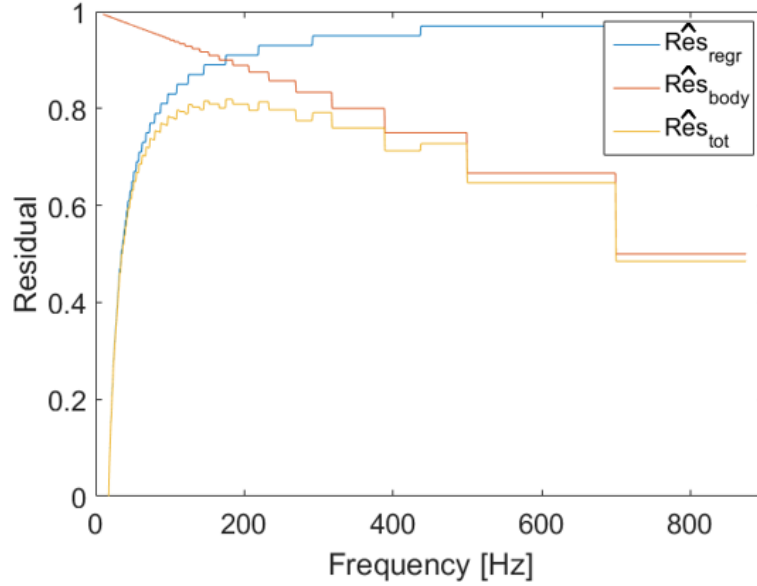


Figure 4.10: Total analytical function and analytical residual curves for the body and the regressor for an observation with $l = 100$.

where l is the number of time samples in the time series, and the exponent c is an unknown variable, found by a `fminsearch` function in Matlab.

Compensation method - Lifting

The third alternative is to use two vectors, D_{body} and D_{regr} , that gives the number of DoF's in the sliding window and regressor for every frequency respectively. For every two consecutive frequencies where the DoF_{body} or DoF_{regr} changes, the difference between the corresponding residual values are added to the the residuals of lower frequencies before the DoF change.

4.2.3 Fine tuning

When model biases are accounted for, the frequency that gives the lowest residual is chosen to be the WBF. Since only a limited number of frequencies are tested originally, the analysis is done once more in a 5% range around the chosen WBF, to obtain a frequency resolution of 0.5 Hz. The process of the frequency analysis can be seen in the flowchart in Figure 4.11.

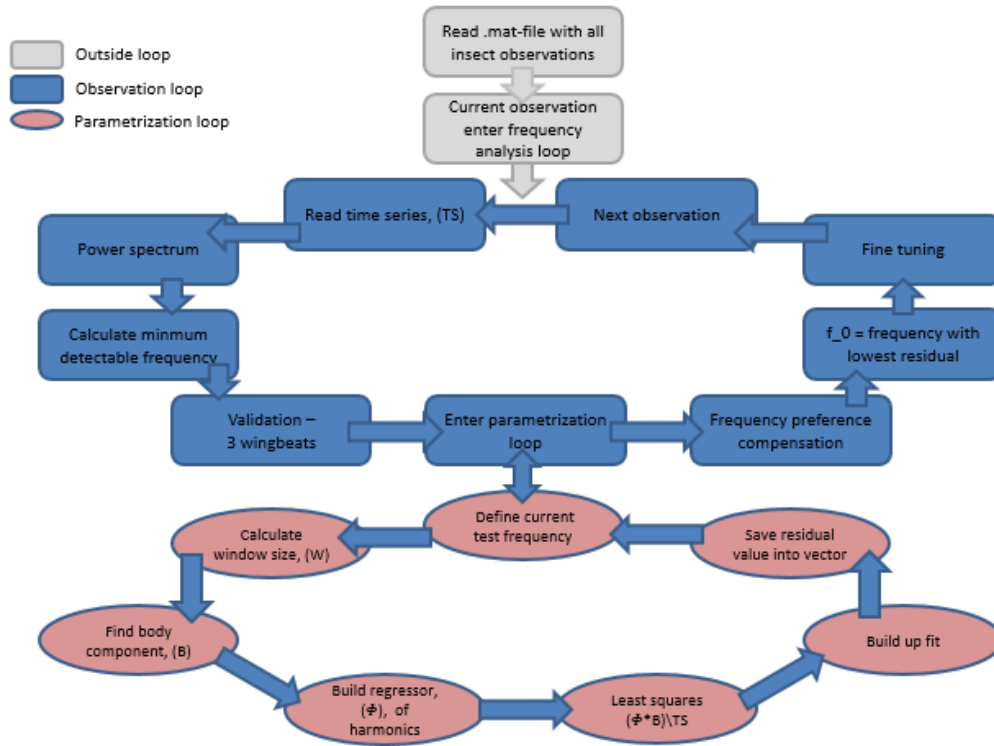


Figure 4.11: The frequency analysis includes extracting the observation data obtained from the main process. If the observation has at least three wing-beats it is analyzed. A model is constructed for a number of test frequencies, and the frequency yielding the lowest residual is selected as the WBF. The model consists of a sliding window that slides through the time series and chooses the lowest value of OCS in the window to build a body vector. The wing beats are constructed using a regressor with a constant and set of harmonic functions, which depends on the test frequency. Using linear regression (least squares method) a fit of the time series is obtained and the sum of squares residual of the fit and the time series is saved in a residual vector with a residual corresponding to every test frequency. Model biasing is compensated for and the frequency that gives the lowest residual after compensation is chosen as WBF. Finally, the WBF is fine tuned in a small range around the chosen WBF.

Chapter 5

FIELD CAMPAIGNS

5.1 Ivory Coast field campaign

The first part of the data was collected during a field campaign in Yamoussoukro in Ivory Coast, using a Scheimpflug Lidar system with a sample frequency of 1750 or 3500 Hz. The system was aligned horizontally and terminated after 516 m. The system and termination positions can be seen in Figure 5.1.



Figure 5.1: Map over the system and termination positions in Ivory Coast.

The data from Ivory Coast is used to investigate how the detection limits in terms of apparent size and OCS change when the sample frequency changes. The data is recorded just before dawn (04.30-06.30 am), at two different days with clear sky condition. This period is chosen since it is the time closest to dawn/dusk when the insects activity peak, where recordings using both sample frequencies without setup problematics and with similar weather conditions could be obtained. The number of observations recorded can be seen in Figure 5.2.

Images of the the system and the campus can be seen in Figure 5.3.

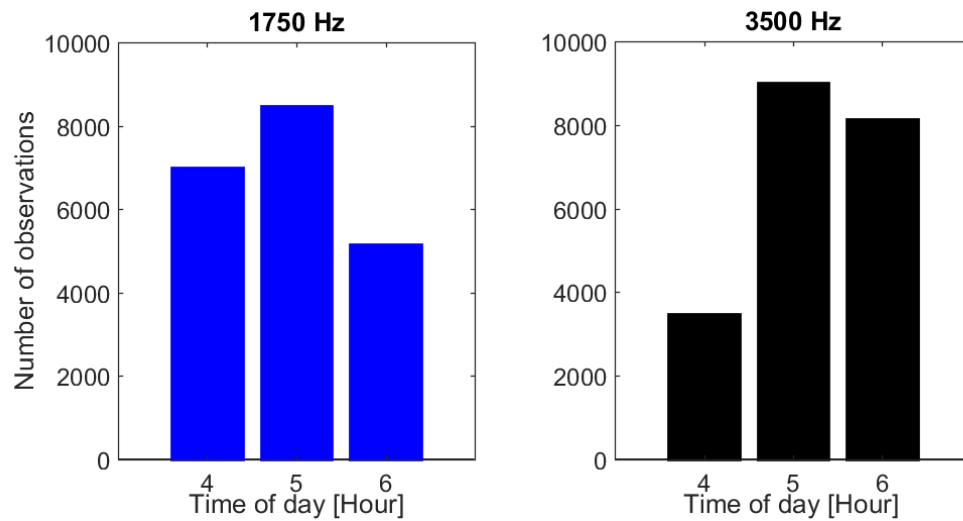


Figure 5.2: Histogram over the recording times for the observation used to investigate the detection limit.



Figure 5.3: a) On our way to eat lunch b) Working with the setup on the roof outside the lab c) Samuel is cutting branches that would interrupt the laser beam. d) African morning sun from the window where the setup was placed. e) Group picture with Professor Jérémie Zoueu who was our contact person, and Benoit Kouakou, a PhD student who works with Lidar.

5.2 Tanzania field campaign

The other part of the data comes from measurements in Lupiro in Tanzania where a Scheimpflug Lidar system was recording data of insect activity during five days. The laser beam was aligned horizontally over a field in the outer part of the village. The setup parameters were identical to the one used in Ivory Coast, except that it was terminated after 595 m and had a constant sample frequency of 3500 Hz. The system and termination positions, as well as the house where the system was placed can be seen in Figure 5.4.

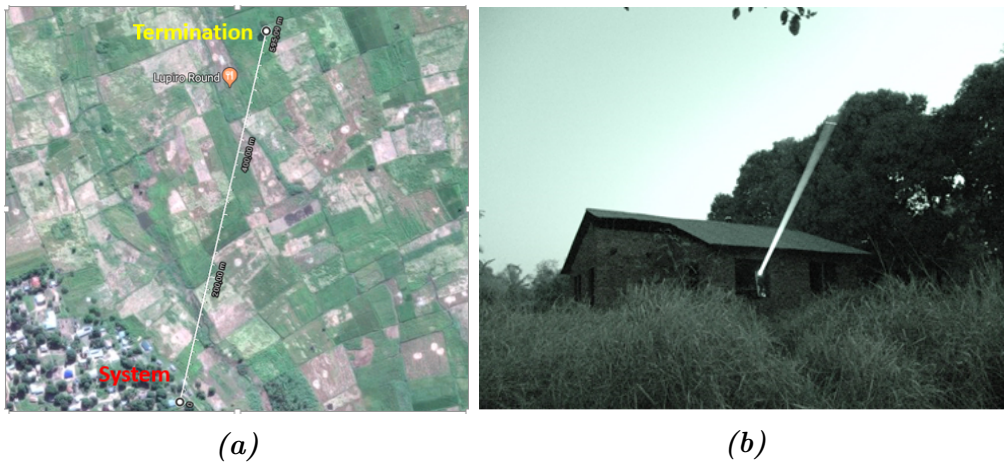


Figure 5.4: a) Map over the system and termination positions in Tanzania. b) Image of the laser beam in Tanzania.

In this thesis, approximately 120 000 insect observations from August 31 to September 1 are used to study the range dependent biases of background light and transit times of the observation. Further, a sample of 1000 observations from dusk (ca 7.00 pm) August 31 is used to study the frequency preferences of the model.

Chapter 6

RESULTS

6.1 Detection limit

The relation between OCS and apparent size can be seen in Figure 6.1, showing that the relation between the apparent size and OCS has the same gradient when using 1750 Hz and 3500 Hz, but the curve for 1750 Hz is shifted towards lower OCS. Studying the distribution of OCS and apparent size in Figure 6.1 it can be seen that the limit of detectable OCS decrease with almost a factor 10 when decreasing the sample frequency from 3500 to 1750, whereas the detectable apparent size is increased with a factor 1.1.

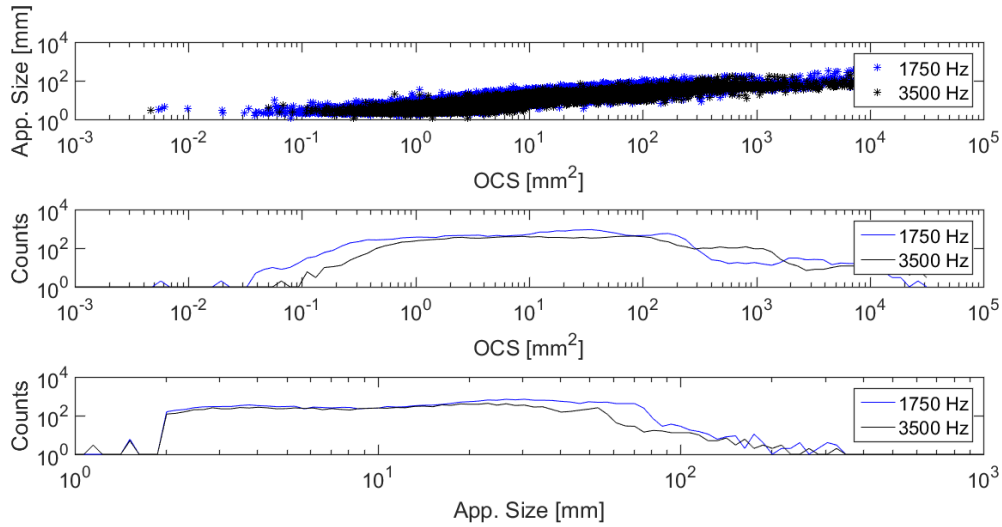


Figure 6.1: Scatter plot of apparent size vs OCS and Biomass spectrum of apparent size and OCS. The limits for detectable OCS decrease with almost a factor 10 when the sample frequency is decreased to half. Further, the detectable apparent size is increased with a factor 1.1.

In Figure 6.2, range dependent biomass spectra can be seen for 1750 and 3500 Hz, showing the change in detectable OCS, while the range distribution is unchanged.

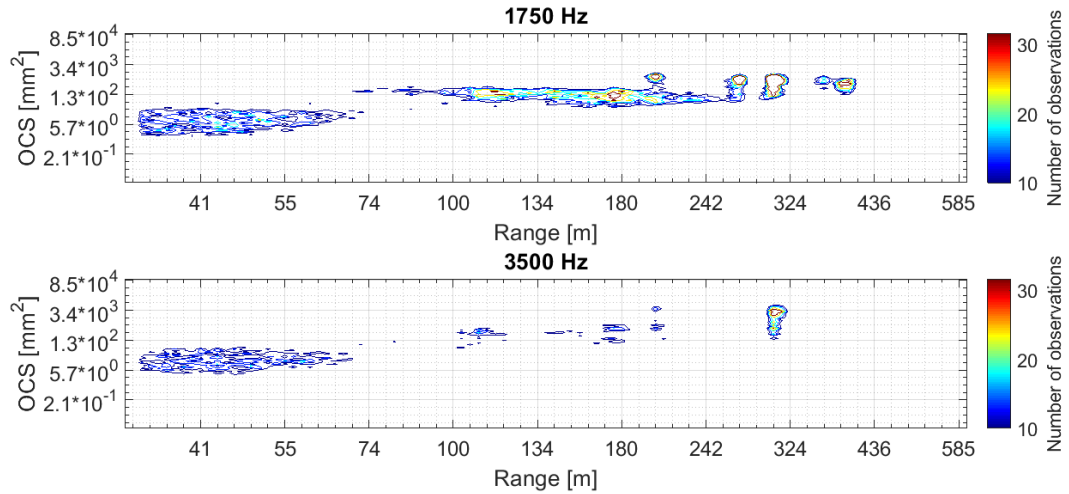


Figure 6.2: Range dependent biomass spectra using a sample frequency of 1750 Hz and 3500 Hz. Using a sample frequency of 1750 Hz, the detectable OCS decrease approximately from 1 mm^2 to 0.5 mm^2 . The sample frequency does not affect the range distribution of observations.

6.2 Range biasing

In Figure 6.3, the relation between transit time and range for the approximately 120000 observations from 18.37 August 31 to 10.37 September 1, 2016, can be seen. Most observations have rather short transit times, ($<50 \text{ ms}$), and more observations are detected at shorter ranges. However, the number of observations with long transit times increase with increasing ranges.

In Figure 6.4, the range dependent background, median, minimum and noise level intensity, averaged from 3 minutes of recordings during dusk and mid day August 31, is plotted. During dusk, the background level is approximately constant, while there is a range dependence during day. Further, a scatter plot between background level and noise level can be seen in Figure 6.4, showing a linear relation between background and noise levels during day.

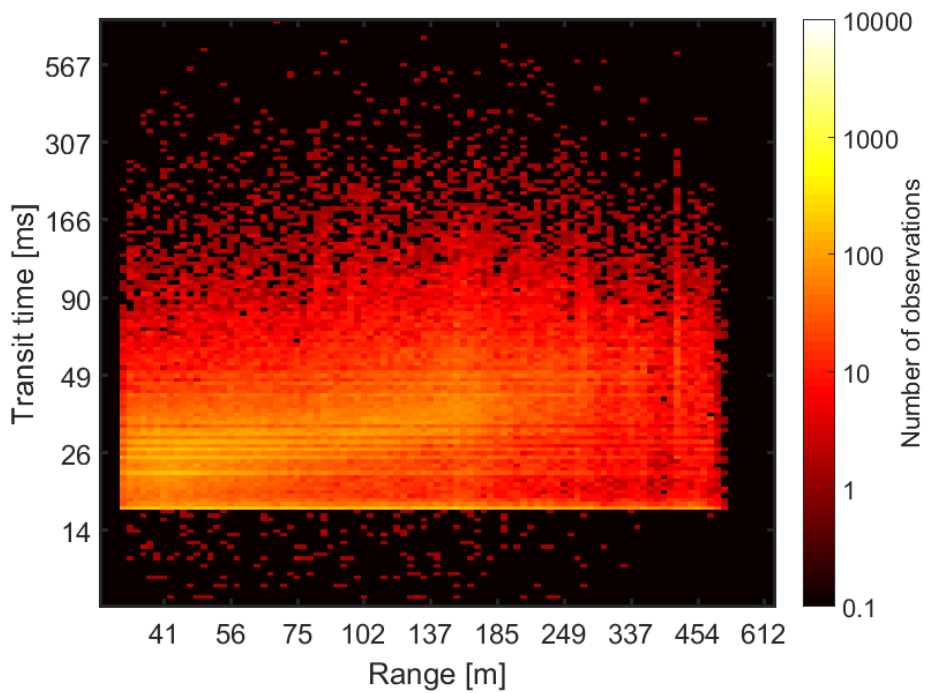


Figure 6.3: Transit time for the almost 120 000 observations during the first two days of the measurements in Tanzania. Most observations are short and are detected close to the system. However, when the range increase, a higher amount of observation with longer transit times are detected.

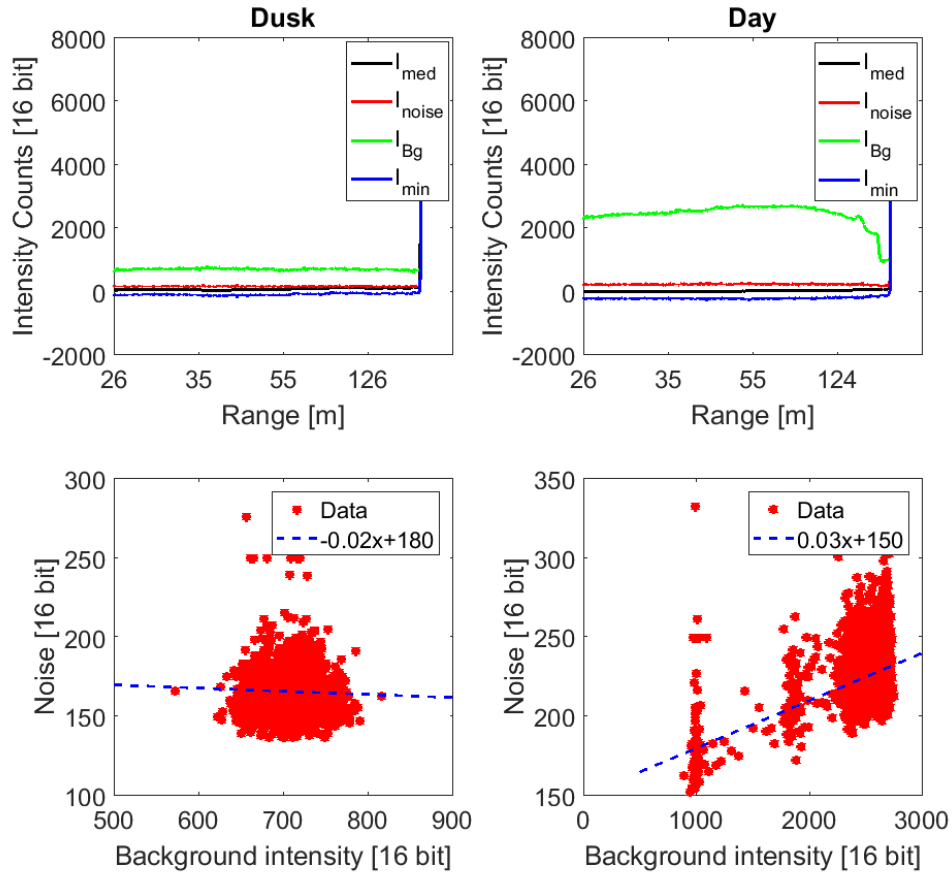


Figure 6.4: Background, median, minimum and noise level intensity as a function of range during day and dusk. Scatter plot between background level and noise level during day and dusk. During dusk, the relation between noise and background level appears to be constant, while there is a linearly dependence during day.

6.3 Frequency preference compensation

In Figure 6.5, residual curves after compensation can be seen for a 30 ms observation with clear wing-beats. In Figure 6.6, 6.7 and 6.8 residual curves after compensation can be seen using the analytical function, analytical function with observation specific Res_{body} , and the lifting method, respectively. The chosen WBF for the three methods are marked in with an arrow.

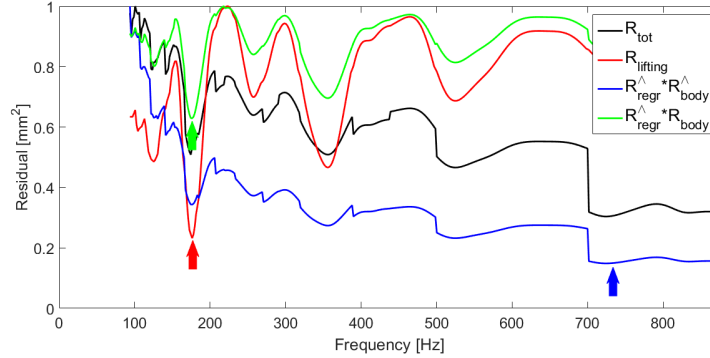


Figure 6.5: Residual curves for the three compensation methods for a clear observation. The chosen WBF is color-coded and marked. The lifting method and the method using the observation body residual chooses the correct WBF whereas the method using analytical function chooses a WBF around 700 Hz.

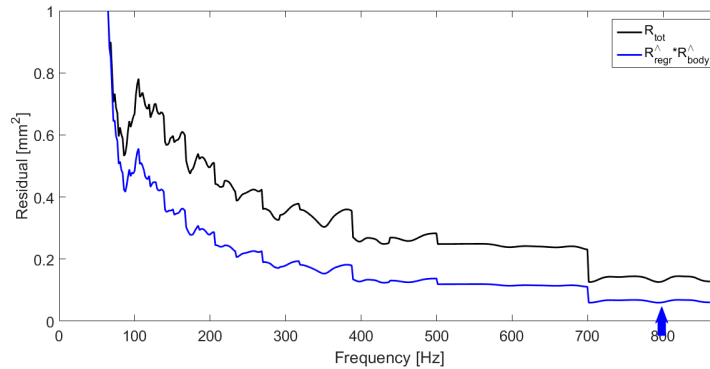


Figure 6.6: Residual curve and compensation curve using an analytical function for example observation 2. The chosen WBF is marked. The steps arising due to a DoF change are still present and the residual have an even higher bias towards higher frequencies.

It can be seen from Figure 6.5 and 6.6 that compensation using an analytical function, results in a residual curve biased towards high frequencies. Further, the function does not succeed in compensation for the steps in the residual curve.

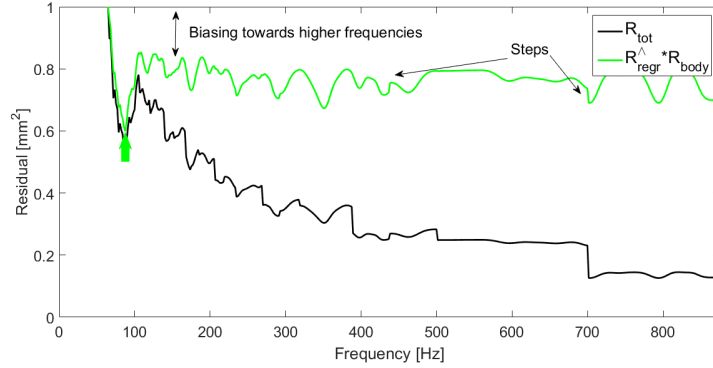


Figure 6.7: Residual curve and compensation curve using analytical $\hat{R}es_{regr}$ and Res_{body} . The chosen WBF is marked. Even after compensation there are remaining steps in the residual and there is a small bias towards higher frequencies.

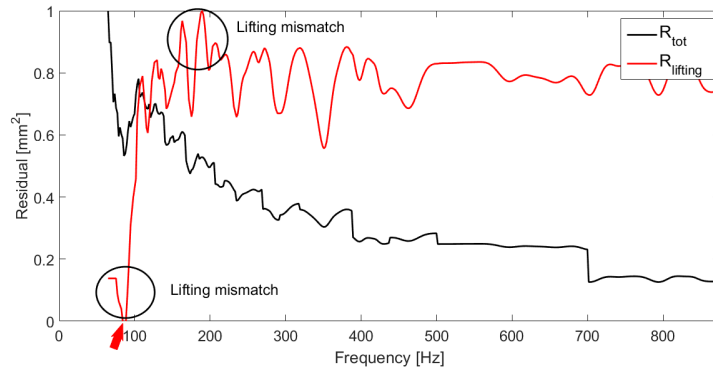


Figure 6.8: Residual curve and compensation curve using the lifting method. The chosen WBF is marked in the power spectrum. An overcompensation using the lifting method can be seen around 100 and 300 Hz, resulting in an increased residual.

Using the observation body residual instead, there are still steps present in some cases, even if they are not as pronounced as when using an analytical function. Further, there is a remaining bias towards higher frequencies. This can be seen in Figure 6.5 and 6.7.

The lifting method is biased towards lower frequencies due to the larger DoF_{regr} for low frequencies, as can be seen in Figure 6.5. Further, in some observations, there are DOF changes in a dip, resulting in overcompensation when lifting the curve up, as around 300 Hz in Figure 6.8.

The distribution of the WBF of 580 observations for the three methods can be seen in Figure 6.9. The method using an analytical function is biased towards frequencies above 700 Hz, i.e. where DOF_{body} changes, whereas the method using an observation body residual and the lifting method gives a more

similar distribution. However, using the observation body residual gives an increased amount chosen WBF around 290 Hz, 438 Hz and 500 Hz, and hence seems to have a higher likelihood of choosing frequencies at DoF changes.

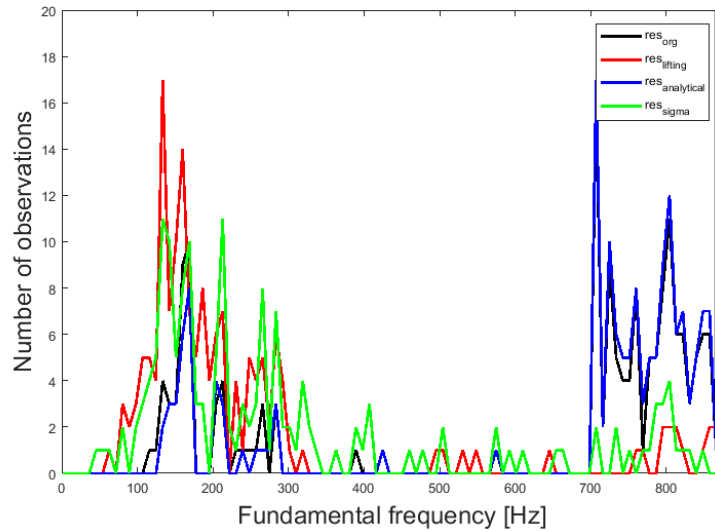


Figure 6.9: WBF distribution for the three compensation methods using 1000 test observations. No compensation, or compensation using the analytical function results in a clear bias toward higher frequencies. The lifting method and the method using the observation body residual results in more observations with lower WBF, which coincides with manual WBF selection. Further, there are small peaks around known DoF changes when using the observation body residual, e.g. round 210 Hz, 290 Hz 500 Hz and 700 Hz.

Chapter 7

DISCUSSION

7.1 Detection limit

Investigating the detection limit of the system shows that there is a connection between the sample frequency and the smallest OCS that can be detected, as seen in Figure 6.1. A lower sample frequency means that the exposure time is longer, the laser pulse energy is higher, and hence it is easier to detect insects giving rise to low intensity signals given that exposure time does not exceed transit time. The shift towards higher apparent sizes using a lower sample frequency can be explained by that the insect have time to cover more range pixels during an exposure.

7.2 Range biasing

From Figure 6.4 it can be seen that there is a clear dependence on range regarding the background level during the day. That might be due to sunlight, clouds, branches that are shadowing the sun etc. However, since mosquitoes in general are active during dusk and dawn and measurements naturally would take place during those times of the day, where the background level seems to be constant, this might not be a problem worth emphasizing.

Considering Figure 6.3, more observations are detected at short ranges, which is an effect of the range-dependent sensitivity.

Further, the number of observations with long transit times increase with range. This is partly due to the expansion of the beam width at longer distances, so an insect flying straight through the beam has a longer transit distance. In reality, some insects are flying along the beam. In that case the insect is considered to be detected on the median range for the observation. Insects that flies along the whole beam and hence have a longer transit time are then considered to be detected at longer ranges than insects that fly along the beam only at short ranges. The main reason to the range dependent transit time is, however, the increasing probe volume, which is the region where the laser

beam overlaps with the field of view of the camera.

7.3 Frequency preference compensation

Analytical function

The main problem with the analytical function is that while the observation residuals vary depending on l as well as the size and shape of the body and wing-beats, the analytical compensation curve only depend on l without taking the shape and size of body and wings into account.

In Figure 4.10, it can be seen how the the stepwise residual increase is equal for all steps of the analytical \hat{Res}_{regr} , which is not the case for the observation residual Res_{regr} . Further, in the analytical function, \hat{Res}_{body} the residual difference for every step is increasing towards higher frequencies, which is not in accordance with the observation residual Res_{body} . Studying Figure 6.5 and 6.6, it can be seen that the shape and step sizes of the uncompensated residual curves can differ between observations to a large extent.

Due to the mismatch of the step-sizes in the observation residual and the compensation curve, steps will still be present in the residual after compensation. This is mainly a problem regarding regressor residual, as the analytical expression \hat{Res}_{regr} have a higher gradient for low frequencies than Res_{regr} . The result is a compensation method that is biased towards higher frequencies, as can be seen in Figure 6.9.

Analytical function using Res_{body}

As can be seen from the results part, using the observation body residual is a suitable compensation method in some cases. The main problem is the mismatch of the step height in the Res_{body} and \hat{Res}_{tot} that results in a small "false peak". In case of short and unclear observations that lack sharp real peaks, the model find one of the false peaks. In Figure 6.9, this is seen as biasing towards frequencies with DoF changes according to Figure 4.8, for example, 700 Hz, 500 Hz, 438 Hz and 210 Hz.

Step lifting

As can be seen from Figure 6.5 and 6.8, the lifting method is a good alternative in some cases. The main problem is the overcompensation that occurs when there is a DoF change that coincides with the WBF or an overtone at low frequencies.

Apart from the frequency preference of the model, there are other factors that will affect the result of the frequency distribution. The data contains lots of insufficient observations that lack clear wing-beats, which often coincide with a short transit time. As can be seen from Figure 4.8 and 4.9, a shorter transit time leads to sharper steps and a sinusoidal behavior in the residual curves. If the observation also lack clear wing-beats, the results is that that either a frequency

corresponding to a DoF change, the frequency of the body contribution, or a random frequency due to the sinusoidal behavior is chosen as WBF.

Chapter 8

CONCLUSIONS AND OUTLOOK

The investigation of the detection limit suggests that a lower sample frequency means a lower detectable OCS which was as expected. However, only two different sample frequencies are compared in the study. To be able to come to significant conclusions the detection limit should be investigated further.

Regarding the range biasing, the most important results are that less observations are detected at longer ranges, and transit times are longer at increasing ranges, which should be kept in mind when investigating transit times of observations.

The parametrization model has shown to be a reasonable method to find the WBF of the time series in the full frequency range, when compensating for the frequency preferences of the model. Unfortunately, neither of the compensation methods that has been tested is problem free.

Presently, the lifting method is the method that gives accurate WBF for most observations. The two remaining problems with the lifting method are when the WBF coincide with a change in DoF, and the low frequency biasing due to the sinusoidal shape of the body time series, is not as frequent as the DoF change biasing in the other two models.

Most of the observations where the model does not find the WBF accurately have short transit time, lack clear wing-beats, etc. Several criteria to sort out low-quality observations, such as shape and size of the body and wing-beats, has been investigated during the year and should be investigated further. Being able to sort out observations that the model is unable to analyze would reduce the biasing that can be seen in the WBF distribution, and facilitate further improvement of the compensation methods.

Bibliography

- [1] World health organisation. www.who.int/gho/malaria/en. Accessed: 2017-09-13.
- [2] K. Meki, K. Yamaguchi, X. Li, Y. Saito, T.D. Kawahara, and A. Nomura. Range-resolved bistatic imaging lidar for the measurement of the lower atmosphere, 1996.
- [3] National geography. <https://www.nationalgeographic.com/animals/invertebrates/group/mosquitoes>. Accessed: 2017-12-16.
- [4] Centers for disease control and prevention. https://www.cdc.gov/malaria/malaria_worldwide/cdc_activities/tanzania.html. Accessed: 2017-09-13.
- [5] Ifakara health institute. <http://ihi.or.tz/project/control-of-malaria-vectors-by-the-\auto-dissemination-of-insecticides>. Accessed: 2017-12-13.
- [6] President's malaria initiative. <https://www.pmi.gov/where-we-work/tanzania>. Accessed: 2017-12-13.
- [7] A.B. Crawford. Radar reflections in the lower atmosphere. *Proc. Inst. Radio Eng.*, 37:404–405, 1949.
- [8] J.R. Riley and D.R. Reynolds. Radar-based studies of the migratory flight of grasshoppers in the middle niger area of mali. *Proc. R. Soc. Lond.*, 204:67–82, 1979.
- [9] G.W. Schaefer. *Insect flight*. John Wiley and Sons, 1976.
- [10] A. Papayannis, D. Balis, V. Amiridis, G. Chourdakis, G. Tsaknakis, C. Zerefos, A.D.A. Castanho, S. Nikovic, S. Kazadzis, and J. Grabowski. Measurements of saharan dust aerosols over the eastern mediterranean using elastic backscatter-raman lidar, spectrophotometric and satellite observations in the frame of the earlinet project. *Atmos. Chem. Phys.*, 5(8):2065–2079, 2005.

- [11] D. Müller, A. Ansmann, I. Mattis, M. Tesche, U. Wandinger, D. Althausen, and G. Pisa. Aerosol-type-dependent lidar ratios observed with raman lidar. *J. Geophys. Res. Atmos.*, 112(D16), 2007.
- [12] A. Papayannis, R. E. Mamouri, V. Amiridis, E. Remoundaki, G. Tsaknakis, P. Kokkalis, I. Veselovskii, A. Kolgotin, A. Nenes, and C. Fountoukis. Optical-microphysical properties of saharan dust aerosols and composition relationship using a multi-wavelength raman lidar, in situ sensors and modelling: a case study analysis. *Atmos. Chem. Phys.*, 12(9):4011–4032, 2012.
- [13] M. R. Perrone, F. De Tomasi, and G. P. Gobbi. Vertically resolved aerosol properties by multi-wavelength lidar measurements. *Atmos. Chem. Phys.*, 14(3), 2014.
- [14] J.R. Bell, P. Aralimarad, K.-S. Lim, , and J.W. Chapman. Predicting insect migration density and speed in the daytime convective boundary layer. *PLoS One*, 8(1), 2013.
- [15] Z.G. Guan, M. Brydegaard, P. Lundin, M. Wellenreuther, A. Runemark, E.I. Svensson, and S. Svanberg. Insect monitoring with fluorescence lidar techniques: field experiments. *Appl. Opt.*, 49(27):5133–42, 2010.
- [16] L. Mei, Z.G. Guan, H.J. Zhou, J. Lv, Z.R. Zhu, J.A. Cheng, F.J. Chen, C. Löfstedt, S. Svanberg, and G. Somesfalean. Insect monitoring with fluorescence lidar techniques: field experiments. *Appl. Phys. B*, 106:733–740, 2016.
- [17] R.J. Allen and W.E. Evans. Laser radar (lidar) for mapping aerosol structure. *Review of Scientific Instruments*, 43(10):1422–1432, 1972.
- [18] V. Matthais, V. Freudenthaler, A. Amodeo, I. Balin, D. Balis, J. Boesenberg, A. Chaikovsky, G. Chourdakis, A. Comeron, A. Delaval, F. D. Tomasi, R. Eixmann, A. Haagaard, L. Komguem, S. Kreipl, R. Matthey, V. Rizi, J. A. Rodrigues, U. Wandinger, and X. Wang. Aerosol lidar intercomparison in the framework of the earlinet project. 1.instruments. *Appl. Opt.*, 43(4):961–976, 2004.
- [19] V. A. Kovalev and W. E. Eichinger. *Elastic lidar: theory, practice, and analysis methods*. John Wiley and Sons, 2004.
- [20] M. Sicard, F. Molero, J. L. Guerrero-Rascado, R. Pedrós, F. J. Expósito, C. Córdoba-Jabonero, J. M. Bolarín, A. Comerón, F. Rocadenbosch, and M. Pujadas. Aerosol lidar intercomparison in the framework of spalinet - the spanish lidar network: Methodology and results. *IEEE Transactions on Geoscience and Remote Sensing*, 47(10):3547–3559, 2009.

- [21] G. Pappalardo, A. Amodeo, A. Apituley, A. Comerón, V. Freudenthaler, H. Linné, A. Ansmann, J. Boesenberg, G. D’Amico, and I. Mattis. Earlinet: towards an advanced sustainable european aerosol lidar network. *Atmospheric Measurement Techniques*, 7:2389–2409, 2014.
- [22] N.C.P. Sharma, J.E. Barnes, T.B. Kaplan, and A.D. Clarke. Coastal aerosol profiling with a camera lidar and nephelometer. *J. Atmos. Ocean. Technol.*, 28(3):418–425, 2011.
- [23] J. Carpentier. Improvements in enlarging or like cameras. *Great Britain Patent No 1139*, 1901.
- [24] T. Scheimpflug. Improved method and apparatus for the systematic alteration or distortion of plane pictures and images by means of lenses and mirrors for photography and for other purposes. *Great Britain Patent No1196*, 1904.
- [25] L. Mei and M. Brydegaard. Atmospheric aerosol monitoring by an elastic scheimpflug lidar system. *Opt. Express*, 23:A1613–A1628, 2015.
- [26] M. Brydegaard, A. Gebru, and S. Svanberg. Super resolution laser radar with blinking atmospheric particles - application to interacting flying insects. *Progress In Electromagnetics Research*, 147:141–151, 2014.
- [27] K. S. Repasky, J. A. Shaw, R. Scheppele, C. Melton, J. L. Carsten, and L. H. Spangler. Optical detection of honeybees by use of wing-beat modulation of scattered laser light for locating explosives and land mines. *Appl. Opt.*, 45(8):1839–1843, 2006.
- [28] D. S. Hoffman, A. R. Nehrir, K. S. Repasky, J. A. Shaw, and J. L. Carlsten. Range-resolved optical detection of honeybees by use of wing-beat modulation of scattered light for locating land mines. *Appl. Opt.*, 46(15):3007–3012, 2007.
- [29] J. A. Shaw, K. S. Repasky, J. L. Carlsten, L. H. Spangler, and D. S. Hoffman. Optical detection of oscillating targets using modulation of scattered laser light, 2009. US Patent 7,511,624.
- [30] E. S. Carlsten, G. R. Wicks, K. S. Repasky, J. L. Carlsten, J. J. Bromenshenk, and C. B. Henderson. Field demonstration of a scanning lidar and detection algorithm for spatially mapping honeybees for biological detection of land mines. *Appl. Opt.*, 50:2112–2123, 2011.
- [31] O. SOTAVALTA. Flight-tone and wing-stroke frequency of insects and the dynamics of insect flight. *Nature*, 170(4338):1057–1058, 1952.
- [32] S.N. Fry, R.Sayaman, and M.H. Dickinson. The aerodynamics of hovering flight in drosophila. *J. Exp. Biol.*, 208:2303–2318, 2005.

- [33] R. Bomphrey. Insects in flight: Direct visualization and flow measurements. *Bioinspiration Biomimetics*, 1:51–59, 2006.
- [34] L.C. Johansson et al. Elytra boost lift, but reduce aerodynamic efficiency in flying beetles. *J.Roy.Soc.Interface*, 9:2745–2748, 2012.
- [35] C. Pennycuik. Predicting wingbeat frequency and wavelength of birds. *J.Exp.Biol.*, 150:171–185, 1990.
- [36] M. Brydegaard. Towards quantitative optical cross sections in entomological laser radar - potential of temporal and spherical parameterizations for identifying atmospheric fauna. *PloS One*, 10(8), 2015.
- [37] I. Potamitis, Rigakis I., and K. Fysarakis. Insect biometrics: Optoacoustic signal processing and its applications to remote monitoring of mcphail type traps. *PLoS One*, 10(11), 2015.
- [38] G.E. Batista, Y. Hao, E. Keogh, and A. Mafra-Neto. Towards automatic classification of flying insects using inexpensive sensors. *10th Int. Conf. Mach. Learning Appl. Workshops*, pages 364–369, 2011.
- [39] A. Moore and R.H. Miller. Automated identification of optically sensed aphid (homoptera: Aphideae) wingbeat eaveforms. *Ann. Entomological Soc. Am.*, 95:1–8, 2002.
- [40] M.A. Caprio, J.X. Huang, M.K. Faver, and A. Moore. Characterization of male and female wingbeat frequencies in the anopheles quadrimaculatus complex in mississippi. *Journal of the American Mosquito Control Association*,, 17(3):186–189, 2001.
- [41] B.J. Arthur, K.S. Emr, R.A. Wyttenbach, and R.R. Hoy. Mosquito (aedes aegypti) flight tones: Frequency, harmonicity, spherical spreading, and phase relationships. *J Acoust Soc Am.*, 135(2):933–41, 2014.
- [42] E. Malmqvist, S. Jansson, S. Török, and M. Brydegaard. Effective parameterization of laser radar observations of atmospheric fauna. *IEEE Journal of Selected Topics in Quantum Electronics*, 22(3):327–334, 2016.
- [43] S. Svanberg. *Atomic and molecular spectroscopy: basic aspects and practical applications;with 14 tables*. Springer Science and Business Media, 2004.
- [44] C.F. Bohren and D.R. Huffman. *Absorption and scattering of light by small particles*. John Wiley and Sons, 2008.
- [45] T. J. Farrel, M. S. Patterson, and B. Wilson. A diffusion theory model of spatially resolved steady-state diffuse reflectance for the noninvasive determination of tissue optical properties in vivo. *Medical Physics*, 19(4), 1992.

- [46] S. L. Jacques. Optical properties of biological tissues: a review. *Physics in Medicine and Biology*, 58(11):R37, 2013.
- [47] W. M. Cornette and J. G. Shanks. Physically reasonable analytic expression for the single-scattering phase function. *Appl. Opt.*, 31(4), 1992.
- [48] D.G.Stavenga. Thin film and multilayer optics cause structural colors of many insects and birds. *Materials Today: Proceedings*, 1:109–121, 2014.
- [49] M. Brydegaard, A. Gebru, C. Kirkeby, S. Åkesson, and H. Smith. Daily evolution of the insect biomass spectrum in an agricultural landscape accessed with lidar. 119:22004, 2016.
- [50] L. Mei and M. Brydegaard. Continuous-wave differential absorption lidar. *Laser and Photonics Reviews*, 9(6):629–636, 2015.
- [51] A. Gebru, E. Rohwer, P. Neethling, and M. Brydegaard. Investigation of atmospheric insect wing-beat frequencies and iridescence features using a multispectral khz remote detection system. *Journal of Applied Remote Sensing*, 8(1):083503–083503, 2014.
- [52] E. A. Robinson. Predictive decomposition of time series with applications to seismic exploration. *Geophysics*, 32:418–484, 1967.
- [53] H. Huang and J. Pan. Speech pitch determination based on hilbert-huang transform. *Signal Processing*, 86(4):792–803, 2006.

APPENDIX

Matlab codes

Raw data processing

```
1 clear all
2 close all
3 clc
4
5 % Define directory of files
6
7 dn='J:\Field Campaign Yamoussoukro\20170409\';
8
9 fn=dir([dn '*.dat']);
10 [~,ind]=sort([fn.datenum]);
11
12 % Define geometry and system parameters
13
14 noFiles=length(fn);
15 noPix=2048;
16 clock=20;
17 SNR=2;
18 tDiff=0;
19
20 marginToTerm=4;
21 shrink=ones(1,3);
22
23 transFoc=0.5;
24 transDiam=0.102;
25
26 recFoc=0.8;
27 recDiam=0.205;
28
29 pixLength=200e-6;
30 pixPitch=14e-6;
31 sensTilt=45;
32
33 sepDist=0.814;
34 termDist=516;%598;
35
36 spotWidth=0.233;
37 spotHeight=0.025;
38 termRefl=0.04;
39
40 P1=polyfit([0 termDist],[transDiam spotWidth],1);
41 P1=@(r) P1(1)*r+P1(2);
42 P2=polyfit([0 termDist],[transDiam spotHeight],1);
```

```

43 P2=@(r) P2(1)*r+P2(2);
44
45 % Define struct to save obs variables
46 observation=[];
47
48 frDark=zeros(noPix,noFiles);
49 frMin=zeros(noPix,noFiles);
50 frMed=zeros(noPix,noFiles);
51 frMax=zeros(noPix,noFiles);
52 frIqr=zeros(noPix,noFiles);
53 frThresh=zeros(noPix,noFiles);
54 frTermIntensity=zeros(1,noFiles);
55 frTermPos=zeros(1,noFiles);
56 frTermWidth=zeros(1,noFiles);
57 frTime=zeros(1,noFiles);
58 frRange=zeros(noPix,noFiles);
59 frProbeVol=zeros(1,noFiles);
60 frOCSconv=zeros(noPix,noFiles);
61 frTermOCS=zeros(noPix,noFiles);
62 frMinDet=zeros(noPix,noFiles);
63 frMaxDet=zeros(noPix,noFiles);
64
65 % Read every file
66 for k=2:noFiles
67
68     %% Opens, reads and shapes the file
69     fid=fopen([dn fn(k).name], 'r', 'b');
70
71     noLines=fread(fid,1, '*uint16');
72     [~,]=fread(fid,1, '*uint16');
73     [~,]=fread(fid,1, '*uint32');
74
75     newLine=fread(fid,1, '*uint8');
76
77     timeStamp=zeros(noLines,1);
78     slotIncr=zeros(noLines,1);
79     slotInd=zeros(noLines,1);
80     Draw=[];
81
82     l=1;
83     while newLine==1
84
85         timeStamp(l)=fread(fid,1, '*uint32');
86         slotIncr(l)=fread(fid,1, '*uint16');
87         slotInd(l)=fread(fid,1, '*uint8');
88         Draw(:,l)=fread(fid,noPix, '*uint16');
89
90         l=l+1;
91         newLine=fread(fid,1, '*uint8');
92     end
93
94     while noLines>size(Draw,2)
95         timeStamp(end)=[];

```

```

96         slotIncr(end)=[];
97         slotInd(end)=[];
98         noLines=noLines-1;
99     end
100     while slotInd(end)~=0
101         Draw(:,end)=[];
102         timeStamp(end)=[];
103         slotIncr(end)=[];
104         slotInd(end)=[];
105         noLines=noLines-1;
106     end
107     fclose(fid);
108
109     Draw=flipud(Draw);
110
111     brightSlots=find(slotInd);
112     darkSlots=find(~slotInd);
113
114     bgr=interp1(timeStamp(darkSlots),Draw(:,darkSlots)',...
115         timeStamp(brightSlots),'linear');
116     D=Draw(:,brightSlots)-bgr;
117     noLines=size(D,2);
118
119     %% Uses the file name to define when the file was recorded
120     name=fn(k).name;
121     temp = datetime(fn(k).datenum, 'ConvertFrom', 'datenum');
122     temp = temp + hours(tDiff);
123     TanzaTime = datenum(temp);
124
125     frTime(k)=TanzaTime;
126
127     %% Retrieve statistics
128     frDark(:,k)=median(Draw(:,darkSlots),2);
129
130     Dsort=sort(D,2);
131     frMin(:,k)=Dsort(:,1);
132     frMed(:,k)=Dsort(:,round(end/2));
133     frMax(:,k)=Dsort(:,end);
134     frIqr(:,k)=Dsort(:,round(3/4*end))-Dsort(:,round(1/4*end));
135     frThresh(:,k)=frMed(:,k)+SNR*abs(frMed(:,k)-frMin(:,k));
136
137     D=D-repmat(frMed(:,k),1,noLines);
138
139     %% Termination
140     [frTermIntensity(k),frTermPos(k)]=max(frMed(:,k));
141     termEnd=frTermPos(k)-1+find(frMed(frTermPos(k):end,k)>...
142         frTermIntensity(k)./2,1,'last');
143     termStart=flipud(frMed(:,k));
144     termStart=frTermPos(k)+1-find(termStart((2049-frTermPos(k)):end)...
145         <frTermIntensity(k)/2,1,'first');
146     frTermWidth(k)=termEnd-termStart+1;
147     frTermIntensity(k)=sum(frMed(termStart:termEnd,k));
148

```

```

149 %% Regions of interest
150 ROImask=zeros(noPix,noLines);
151 ROImask(1:(frTermPos(k)-marginToTerm*frTermWidth(k)),:)=1;
152 FOVregion=1:(frTermPos(k));
153
154 %% Range vector
155 termPixDist=1/(1/recFoc-1/termDist);
156 pix_y=sind(sensTilt)*pixPitch*(noPix/2-(1:noPix)');
157 termPix_z=sqrt(termPixDist^2-pix_y(frTermPos(k))^2);
158 pix_z=cosd(sensTilt)*pixPitch*(1:noPix)';
159 pix_z=flipud(pix_z)+termPix_z;
160 pix_z=pix_z-(pix_z(frTermPos(k))-pix_z(end));
161
162 termAng=atand(sepDist/termDist);
163 termPixAng=atand(pix_y(frTermPos(k))/pix_z(frTermPos(k)));
164 alpha=termAng-termPixAng;
165
166 pixAng=atand(pix_y./pix_z);
167 rAng=pixAng+alpha;
168
169 frRange(:,k)=sepDist./tand(rAng);
170 dr = interp1((frRange(1:(end-1),k)+frRange(2:end,k))/2,diff(frRange(:,k)),...
171     frRange(:,k),'pchip','extrap');
172
173 %% Probe Volume
174 beamWidth=P1(frRange(FOVregion,k));
175 beamHeight=P2(frRange(FOVregion,k));
176 FOVwidth=pixLength*frRange(FOVregion,k)./pix_z(FOVregion);
177 FOVheight=sind(sensTilt)*pixPitch*frRange(FOVregion,k)./pix_z(FOVregion);
178
179 probeVolWidth=min(beamWidth,FOVwidth);
180 probeVolHeight=min(beamHeight,FOVheight);
181
182 probeVolume=dr(FOVregion).*probeVolWidth.*probeVolHeight;
183 frProbeVol(k)=sum(probeVolume(1:frTermPos(k)));
184
185 %% OCS calibration
186 frTermOCS(k)=probeVolWidth(frTermPos(k))*probeVolHeight(frTermPos(k))*termRefl;
187 frOCsconv(:,k)=frTermOCS(k)*frRange(:,k).^2./(frMed(:,k)*...
188     frRange(frTermPos(k),k)^2);
189 frOCsconv((length(FOVregion)+1):end,k)=0;
190
191 OCsmap=D.*repmat(frOCsconv(:,k),1,noLines);
192
193 frMinDet(:,k)=frOCsconv(:,k).*(frThresh(:,k)-frMed(:,k));
194 frMaxDet(:,k)=frOCsconv(:,k).*((2^16-1)-frMed(:,k));
195
196 %% Find insect observations
197 Dmask=(D>repmat(frThresh(:,k)-frMed(:,k),1,noLines)).*ROImask;
198 Dmask=imerode(Dmask,shrink);
199 Dmask=imdilate(Dmask,grow);
200
201 T=bwconncomp(Dmask);

```

```

202
203     %% Extract and parameterize observations
204     entry=[];
205     if T.NumObjects>0
206         for l=1:T.NumObjects
207             [rr,tt]=ind2sub(size(D),T.PixelIdxList{l});
208
209             entry(l).fn=k;
210
211             entry(l).rInd=min(rr):max(rr);
212             entry(l).tInd=min(tt):max(tt);
213
214             entry(l).rtMap=OCSmap(entry(l).rInd,entry(l).tInd).*...
215                 Dmask(entry(l).rInd,entry(l).tInd);
216             entry(l).bsTS=sum(entry(l).rtMap,1);
217             entry(l).time=datevec(frTime(k))+[0 0 0 0 0 timeStamp...
218                 (brightSlots(round(mean(entry(l).tInd))))];
219             entry(l).time=datetime(entry(l).time);
220             entry(l).dt=length(entry(l).tInd)/fs;
221
222             entry(l).centralPix=round(mean(entry(l).rInd));
223
224             entry(l).range=frRange(entry(l).centralPix,k);
225
226             [~,entry(l).pixCoverage]=mode(tt);
227             entry(l).appSize=sind(sensTilt)*pixPitch*entry(l).pixCoverage*...
228                 entry(l).range/sqrt(pix_y(entry(l).centralPix)^2+...
229                 pix_z(entry(l).centralPix)^2);
230         end
231
232         observation=[observation entry];
233
234     end
235
236     %% Saving
237     disp('Saving...')
238     dn2 = 'C:\Users\Alexandra\Documents\Master_Matlab\Master_matFilesElf\FA_in\';
239     save([dn2 'FA_in_Elf14_300short.mat'],'observation','frDark','frMin','frMed',...
240         'frMax','frIqr','frThresh','frTermIntensity','frTermPos','frTermWidth',...
241         'frTime','frRange','frProbeVol','frOCSconv','frTermOCS','frMinDet','frMaxDet')
242     disp('Saved.')

```

Frequency analysis

```
1 % Required variables for this function: observation time series,
2 %sample frequency and noise amplitude
3 function eventOut = FA(event)
4
5 t_ser = event.OCSevent';
6 l_event = length(t_ser);
7 f_sample = event.f_sample;
8 max_t = l_event/event.f_sample;
9 t = linspace(0,max_t,l_event);
10
11 %% Create Pow spec and freq vectors
12
13 % max meas freq is Nyqvist frequency
14 Freq_max = event.f_sample/2;
15
16 % min 3 wingbeats
17 Freq_min = 3/(max_t);
18
19 % Create test frequency vector
20 fminind = ceil(Freq_min/(Freq_max - 1)/500);
21 Freq_test = linspace(Freq_min,Freq_max,501-fminind);
22
23 %% Enter freq an loop, if the event fulfill the conditions
24
25 if findpeaks(t_ser) > 2
26
27     % Loop through and find np harmonics
28
29     for f = 1:length(Freq_test)
30 %
31         period = 2*Freq_max/Freq_test(f);
32         body_np = bodyFilt(t_ser,Freq_test(f),Freq_max,event.half_noise);
33         wings_np = t_ser - body_np;
34
35         % Build regressor
36         harm_np = [ones(l_event,1)];
37
38         for h = 1:floor((Freq_max/Freq_test(f)))
39
40             harm_np = [harm_np sin(2*pi*h*Freq_test(f)*t)' cos(2*pi*h*Freq_test(f)*t)'];
41
42         end
43
44         % Body weighing
45         regr_np = harm_np.*repmat(body_np,[1 size(harm_np,2)]);
46
47         coeff_np = regr_np\t_ser;
48         coeff_wing = harm_np\t_ser;
49         coeff_body = body_np\t_ser;
50
```

```

51     t_ser_fit_np = regr_np*coeff_np;
52     resi_np(f) = sum((t_ser - t_ser_fit_np).^2)/l_event;
53
54     wingfit = harm_np*coeff_wing;
55     resiwing(f) = sum((t_ser - wingfit).^2)/l_event;
56
57     bodyfit = body_np*coeff_body;
58     resibody(f) = sum((t_ser - bodyfit).^2)/l_event;
59
60     end
61
62     %% Preference compensation
63
64     h = floor(Freq_max./Freq_test);
65     DOF_regr = 1+(2.*h);
66
67     W = round(2.*Freq_max./Freq_test);
68     DOF_wind = l_event./W;
69
70     Res_regr = (1-(DOF_regr./l_event));
71     Res_wind = (1-(DOF_wind./l_event));
72     Res_tot = Res_regr.*Res_wind;
73
74     % Alternative 1 - Analytical function
75
76     Res_1 = resi_np./Res_tot;
77
78     % Alternative 2 - resibody
79
80     resi_p = resi_np./resibody;
81     c = resi_p(1);
82     height = resi_p;
83     X = DOF_regr./l_event;
84     fitcoeff = fminsearch(@wingan,[c,4],[],X,l_event,height);
85     height = (1-X).*fitcoeff(1).*(l_event.^(1/fitcoeff(2)));
86
87     Res_2 = resi_p./height;
88
89     % Alternative 3 - lifting it up
90
91     Res_3 = resi_np;
92
93     for u = 1:length(DOF_wind)-1
94
95         if DOF_wind(u) ~= DOF_wind(u+1)
96
97             if u == 1
98
99                 Res_3(u) = Res_3(u) + (Res_3(u+1) - Res_3(u));
100
101             else
102                 Res_3(1:u) = Res_3(1:u) + (Res_3(u+1)-Res_3(u));
103                 Res_3(u) = (Res_3(u-1) + Res_3(u+1))/2;

```

```

104
105     end
106 end
107
108     if DOF_regr(u) ~= DOF_regr(u+1)
109
110
111         if u == 1
112
113             Res_3(u) = Res_3(u) + (Res_3(u+1) - Res_3(u));
114
115         else
116             Res_3(1:u) = Res_3(1:u) + (Res_3(u+1)-Res_3(u));
117             Res_3(u) = (Res_3(u-1) + Res_3(u+1))/2;
118
119         end
120
121     end
122 end
123
124 % Find min res - change res dep on method
125 res = Res_3
126 [res_fin,f0ind] = min(res);
127 f0_p = Freq_test(f0ind);
128
129
130 %% Fine tuning
131
132 test_reg = linspace(0.95*f0_p,1.05*f0_p,round((1.05*f0_p-0.95*f0_p)/0.5));
133
134
135 for f = 1:length(test_reg)
136
137     body = bodyFilt(t_ser,test_reg(f),Freq_max,event.half_noise);
138     wings = t_ser - body;
139
140     harm = [ones(1_event,1)];
141
142     for h = 1:floor((Freq_max/test_reg(f)))
143
144         harm = [harm sin(2*pi*h*test_reg(f)*t) ' cos(2*pi*h*test_reg(f)*t)'];
145
146     end
147
148     regr = harm.*repmat(body_np,[1 size(harm,2)]);
149
150     coeff = regr\wings;
151
152     t_ser_fit = regr*coeff;
153     resi_fine(f) = sum((wings - t_ser_fit).^2)/1_event;
154
155 end
156

```



```

157     [res_ft, ind_ft] = min(resi_fine);
158     f0 = test_reg(ind_ft);
159
160
161     %% Build up correct fit
162
163     body_p = bodyFilt(t_ser, f0, Freq_max, event.half_noise);
164     wings_p = t_ser - body_p;
165
166     DC = ones(1_event, 1);
167     harm_p = [DC];
168
169     for h = 1:floor(Freq_max/f0_p)
170
171         harm_p = [harm_p sin(2*pi*h*f0_p*t)' cos(2*pi*h*f0_p*t)'];
172
173     end
174
175     regr_p = harm_p.*repmat(body_p, [1 size(harm_p, 2)]);
176
177     coeff_p = regr_p \ wings_p;
178
179     t_ser_fit_p = regr_p * coeff_p;
180     t_ser_res_p = sum((wings_p - t_ser_fit_p).^2) / 1_event;
181
182     %% Save event parameters to event struct
183     event.harmDOF = DOF_regr(f);
184     event.bodyDOF = DOF_wind(f);
185
186     ...
187 else
188     event.harmDOF = NaN;
189     event.bodyDOF = NaN;
190     ...
191 end
192
193
194 eventOut = event;

```

Body time series

```
1 % Sliding window creating body time series
2 % Requires, time series, current test WBF, f_s and noise amplitude
3 function bodyVect=bodyFilt(ts,f0,fs,noiseAmp)
4
5 L=round(2*fs/f0);
6
7 odd=mod(L,2); % Check if window is even or odd sized
8
9 if odd
10
11     tsb=imerode(ts,ones(L,1)); % Sliding minimum
12
13 else
14
15     tsb=imerode(ts,ones(L,1)); % Sliding minimum
16
17     tsb=(tsb(1:(end-1))+tsb(2:end))/2; % interpolation
18
19     tsb=[tsb(1); tsb];
20
21 end
22
23 W=normpdf(0:L,L/2,L/(4*sqrt(2*log(2))))/sum(normpdf(0:L,L/2,L/(4*sqrt(2*log(2))))); % Ga
24 tsb = conv(tsb,W,'same');
25
26 bodyVect=tsb+noiseAmp;
```